Bulk and interfacial modes of instability in channel flow of thixotropic-viscoelasto-plastic fluids with shear-banding

Hugo A. Castillo and Helen J. Wilson
Mathematics Department, University College London
Gower Street, London WC1E 6BT, UK

June 11, 2020

Abstract

We carry out a linear stability analysis of the generalised BMP model, which incorporates the shear-banding phenomenon into flows of thixotropic-viscoelasto-plastic fluids: common behaviours observed in wormlike micellar solutions. We introduce a new dimensionless parameter governing shear-banding, and find that when a flow is unstable in the absence of shear-banding, this parameter has a stabilising effect. Above a critical value of the shear-banding parameter, shear bands appear in the flow gradient direction. Here two different modes of instability are observed: a bulk mode (which is the same as that seen in the absence of shear banding) and an interfacial mode. We found that the former dominates over the latter at low values of the shear-banding parameter, but the interfacial instability becomes dominant at very high values of the parameter. In particular, the interfacial modes are more unstable in flows where the low shear band has almost constant viscosity. The two modes of instability depend on different material timescales: interfacial modes become more dangerous if the interface location is near the channel wall, which is seen when the structural relaxation time is much larger than that of plasticity, while bulk modes (as seen in previous work) are highly unstable if the timescale of viscoelasticity is much longer than both those of plasticity and thixotropy.

1 Introduction

In our previous theoretical work [9], we studied elastic instabilities in planar Poiseuille flow of thixotropic-viscoelasto-plastic fluids, and we found that insta-

bility is seen when viscoelastic effects dominate. On the other hand, thixotropy has a stabilising effect. More importantly, we found that the structural relaxation time determines the growth rate of instability.

In the present work, we extend the scope of the fluids we can consider by including the shear-banding phenomenon in the flows of thixotropic-viscoelasto-plastic fluids. This kind of complex rheological behaviour has been experimentally observed multiple times in wormlike micellar solutions. These fluids have been the center of numerous experimental and theoretical studies, and this is because they are of industrial relevance as their use is commonly found in household items, in the oil industry, and many other applications such as drag reducing agents. These solutions can show fascinating rheological properties; for instance, in steady simple shear flow, the fluid exhibits a linear dependence of the shear stress on the shear rate (i.e. Newtonian-like behaviour with high viscosity) at very low shear rates. An increase in shear rate will cause a drop in viscosity (shear-thinning), as there is a strong dependence of the viscosity (and thus, of the microstructure) on the applied shear rate. Above a critical value of the shear stress, the initially homogeneous flow becomes unstable, which will lead the system to separate into two different bands with different internal structure and different shear-rate values. These two bands are separated by an interface whose normal is in the flow-gradient direction. This phenomenon is called *shear-banded* flow or *shear-banding* transition, which describes a transition between a homogeneous and non-homogeneous state of flow. At very high shear rates, the flow becomes homogeneous again and the fluid will display a single, but a smaller viscosity.

The critical stress value described above is called the *stress plateau* σ_p: below this value, we observe entangled networks of micellar solutions; when the stress applied is $\sigma = \sigma_p$, separation of bands occur and they coexist at this point, and above this stress value, the majority of entanglements will be destroyed, leading to flow-oriented linear wormlike chains. The coexistence of the low and high viscosity bands has been confirmed by different experimental techniques [5, 31, 4, 12].

However, as reported in the literature, shear-banded fluids are susceptible to the development of elastic instabilities, and thus, it is of great interest to predict the flow conditions for which the flow of these fluids become highly unstable in order to avoid incorrect measurements of rheological data and in order to predict difficulties in industrial flows. These flow instabilities driven by elasticity have been observed in micellar solutions in different geometries, such as Taylor-Couette rheometers [15, 34, 27], cone-and-plate [6], microchannel [35, 25, 21] and pipe flows [42], to name a few.

Early work by López-González *et al.* [30, 29, 24] demonstrated, using magnetic-resonance velocimetry techniques, the existence of erratic motions in the interface between bands in Couette flow, which are correlated to shear stress fluctuations. By analysing individual velocity profiles, they also showed that the magnitude of local velocity fluctuations was much larger in the high shear-rate

band. Similar results were observed by Manneville *et al.* [33, 28]. In these experiments, most of the data revealed a strong correlation between the slip dynamics at the moving wall and the bulk dynamics. However, they could not distinguish which of these phenomena was driving the other one.

For the case of microchannels, Nghe *et al.* [35] studied the shear-banding flow of a micellar surfactant solution and they found an instability of the interface between the bands. More specifically, they observed undulations along the interface in the gradient/neutral plane. Similar behaviour was observed in pipe Poiseuille flow of a wormlike micellar solution [42].

These experimental observations have motivated a huge number of rheologists to develop theoretical research. For instance, linear stability analysis of the diffusive Johnson-Segalman model in both planar and curved Couette geometries was carried out by Fielding [17]. She showed that, depending on the level of the cell curvature and on the material's constitutive properties, it is possible to find either a bulk viscoelastic Taylor-Couette instability in the high shear rate band driven by large values of N_1, or an instability of the diffuse interface between the bands driven by a jump in N_2 across it. Nicolas & Morozov [36] found similar results in Taylor-Couette flow: they found that at the beginning of the stress plateau (where the proportion of the high shear rate band is small), an interfacial instability is present, while most of the plateau is occupied by a bulk instability.

Unstable shear banded flows have also been studied theoretically by Fielding & Wilson [16, 39] in planar Couette flow of both diffusive and non-diffusive Johnson-Segalman fluids. For the non-diffusive case, they found that the flow is unstable to long waves for most of the arrangements between the bands, while weak diffusion has a small stabilising effect. In addition, they identified two key ingredients that cause the interfacial instability predicted by them: a jump in the first normal stress difference at the interface and a discontinuity in the shear rate.

The stability of pressure-driven channel flows of shear-banding micellar solutions was also studied by Wilson & Filelding [18] and by Cromer *et al.* [11]; the former used a diffusive Johnson-Segalman model and the latter a two-species reptation-reaction network model. Both works predicted an interfacial instability similar to the one described in [16, 39]. The disadvantage of these works, are the limitations of the models used by them; although the diffusive-Johnson-Segalman model is able to predict non-monotonic curves and it has been used to understand some features of the band formation, this model cannot describe the breaking and reformation processes of these micellar systems under flow, which are important ingredients of a model that need to be considered if one wishes to accurately describe other highly non-linear behaviours of micellar solutions. On the other hand, Cromer's model is able to describe linear and non-linear rheological behaviour prior to the onset of shear-banding. It also works well in predicting start-up shearing flow, cessation of steady shear flow, among others, but fails to predict N_2 and to describe the onset of the stress plateau observed

in experiments.

Lastly, a recently published paper by Renardy *et al.* [38] studied the stability of two-dimensional plane Couette flow of a viscoelastic fluid with thixotropic yield stress behaviour that exhibits the shear-banding phenomenon. Using a thixotropic model that can describe non-monotonic behaviour of the flow curve, and in which the yield stress arises naturally as a limiting case of the model itself [26, 37], they found a bulk mode in the yielded phase (i.e. in the high-shear rate band) which is present even in the absence of shear banding. When an interface appears, interfacial and bulk modes are present, but the latter become the dominant mechanism of instability in shear-banded flows. They also showed that interfacial modes are driven by a jump in the first normal stress difference across the interface between the bands.

In the present work, we use a much more realistic constitutive model, which is an extension of the model used in our previous work [9]: *the generalised BMP model*, which is able to predict the shear-banding phenomenon of micellar solutions, along with thixotropic, viscoelastic and plastic behaviours. We introduce this model in section 2 and show the behaviour in simple shear flow, where we illustrate the characteristic flow curve of shear-banded fluids predicted by the model in section 2.2. The dimensionless governing equations and the dimensionless groups are derived in section 2.3. We show the base-state quantities and illustrate the velocity and fluidity profiles for different model parameter values in 3.1. The perturbed governing equations, the boundary conditions and a description of the numerical methods to be used to solve our stability problem are found in sections 3.3 and 3.4, respectively. Finally, we show our results in section 4 and draw conclusions in section 5.

2 Model fluid: The generalised BMP model

2.1 Governing equations

In order to study the flow instabilities of TVEP fluids that exhibit the shear-banding phenomenon, we consider the *generalised BMP* model [32], which was derived using an extended irreversible thermodynamics formalism. The set of equations for this model consists of a viscoelastic constitutive equation coupled to an evolution equation of a *structural parameter* (fluidity φ or the inverse of viscosity, which is used to measure the level of microstructure of a fluid, such as molecular entanglements, network junctions, or micelle length) that represents the process in which the internal structure of the fluid is modified by an external flow.

For this model, the fluid flows with velocity $\underline{u}$, and its stress tensor $\underline{\underline{\sigma}}$ evolves

according to the Upper-Convected Maxwell (UCM) model:

$$\underline{\underline{\sigma}} + \frac{1}{G_0\varphi} \overset{\nabla}{\underline{\underline{\sigma}}} = \frac{2}{\varphi}\underline{\underline{D}}, \tag{1}$$

where G_0 is the elastic modulus, and $\underline{\underline{D}}$ is the symmetric part of the flow gradient tensor $\underline{\nabla}\,\underline{u}$:

$$\underline{\underline{D}} = \frac{1}{2}\left[\underline{\nabla}\,\underline{u} + \underline{\nabla}\,\underline{u}^{\top}\right] \quad D_{ij} = \frac{1}{2}\left[\frac{\partial u_i}{\partial x_j} + \frac{\partial u_j}{\partial x_i}\right]. \tag{2}$$

The upper-convected derivative that appears in the left side of (1) is defined as:

$$\overset{\nabla}{\underline{\underline{\sigma}}} = \frac{D\underline{\underline{\sigma}}}{Dt} - \underline{\underline{\sigma}} \cdot (\underline{\nabla}\,\underline{u}) - (\underline{\nabla}\,\underline{u})^{\top} \cdot \underline{\underline{\sigma}}, \tag{3}$$

where D/Dt denotes the material derivative (for any scalar, vector or tensor quantity A):

$$\frac{DA}{Dt} = \frac{\partial A}{\partial t} + \underline{u} \cdot \underline{\nabla} A. \tag{4}$$

Equation (1) is coupled to a Fredrickson's-like equation [19], which describes the process in which a fluid undergoes a process of structure modification characterised by destruction and reformation processes:

$$\frac{D\varphi}{Dt} = \frac{1}{\lambda}(\varphi_0 - \varphi) + K(II_D)(\varphi_\infty - \varphi)\underline{\underline{\sigma}} : \underline{\underline{D}}. \tag{5}$$

The first term of the right side of the equation represents the reformation process (build-up of viscosity or breakdown of fluidity), where λ is the *structural relaxation time* and φ_0, the plateau fluidity observed at low shear rates; and the second term is the destruction process (breakdown of viscosity or build-up of fluidity), described by K, a rate parameter for structure destruction, φ_∞, the fluidity at high shear rates, and $\sigma_{ij}D_{ij}$, the rate of energy dissipation in the fluid.

The main difference between the model we will be using here and the one used in our previous paper [9] is that in equation (5), the destruction parameter K is a function of the second invariant of the rate of deformation tensor $II_D = 2\,D_{ij}\,D_{ij}$ and adopts, in the simplest version, the following form (see [3, 1]):

$$K = K_0\left(1 + \vartheta\sqrt{II_D}\right). \tag{6}$$

Here, K is a first order linear expression where K_0 is a kinetic parameter at zero-shear strain, and ϑ is a coefficient that can be determined experimentally and is known as *shear-banding* parameter, which, according to extended irreversible thermodynamics principles, will determine the location of the *stress plateau* observed in fluids that exhibit formation of shear bands. In simple shear flow, equation (6) can be written as $K = K_0(1 + \vartheta\dot{\gamma})$. In the absence of the shear-banding parameter ($\vartheta = 0$), we recover the original model [2].

Finally, the constitutive equations (1) and (5) are coupled with the continuity and momentum equations (in the absence of external forces such as gravity):

$$\underline{\nabla} \cdot \underline{u} = 0 \tag{7}$$

$$\rho \left(\frac{\partial \underline{u}}{\partial t} + \underline{u} \cdot \underline{\nabla u} \right) = -\underline{\nabla} P + \underline{\nabla} \cdot \underline{\underline{\sigma}}, \tag{8}$$

where ρ is the fluid density and P is the pressure.

2.2 Behaviour in steady simple shear

For simple steady shear flow, and considering cartesian coordinates $\underline{u} = \dot{\gamma} y \underline{e}_x$ with $\dot{\gamma} > 0$, equations (1) and (5) become:

$$\underline{\underline{\sigma}} = \begin{pmatrix} 2\,\dot{\gamma}^2\, G_0^{-1}\, \varphi^{-2} & \varphi^{-1}\dot{\gamma} \\ \varphi^{-1}\dot{\gamma} & 0 \end{pmatrix} \tag{9}$$

$$0 = \frac{1}{\lambda}(\varphi_0 - \varphi) + K_0(1 + \vartheta\,\dot{\gamma})(\varphi_\infty - \varphi)\,\sigma_{12}\,\dot{\gamma}. \tag{10}$$

Combining equations (10) and (9), we get a cubic equation for the fluidity:

$$\varphi^3 + a_0\,\varphi^2 + b_0\,\varphi - c_0 = 0 \tag{11}$$

$$a_0 = \frac{1}{\sigma_{12}\,\vartheta} - \varphi_\infty \qquad b_0 = \frac{1}{K_0\,\lambda\,\vartheta\,\sigma_{12}^3} - \frac{\varphi_\infty}{\sigma_{12}\,\vartheta} \qquad c_0 = \frac{\varphi_0}{K_0\,\lambda\,\vartheta\,\sigma_{12}^3}. \tag{12}$$

Additionally, using Cardano's method, we derive the following expressions:

$$Q_0 = \frac{3\,b_0 - a_0^2}{9} \qquad R_0 = \frac{9\,a_0\,b_0 - 27\,c_0 - 2\,a_0^3}{54} \qquad H_0 = Q_0^3 + R_0^2. \tag{13}$$

For fixed value of shear stress σ_{12}, and a given set of parameters K_0, λ, φ_0, φ_∞ and ϑ, we can solve the cubic equation, for which we can either get a positive real root and two imaginary ones (if $H_0 > 0$), three real roots but two of them are equal ($H_0 = 0$) and three different real roots if $H_0 < 0$. The full analytic solutions of the cubic equation (11) can be found in [7], where authors demonstrated, using chaos theory and irreversible thermodynamics, that the *shear stress plateau* σ_p satisfies the condition $R_0 = 0$.

When solving equations (9) and (11), the simple shear flow material functions (viscosity η, shear stress σ_{12} and the first normal stress difference coefficient Ψ_1) can be obtained as follows:

$$\eta = \varphi^{-1} \qquad \sigma_{12} = \eta\,\dot{\gamma} \qquad \Psi_1 = \frac{\sigma_{11} - \sigma_{22}}{\dot{\gamma}^2} = 2\,G_0^{-1}\,\eta^2. \tag{14}$$

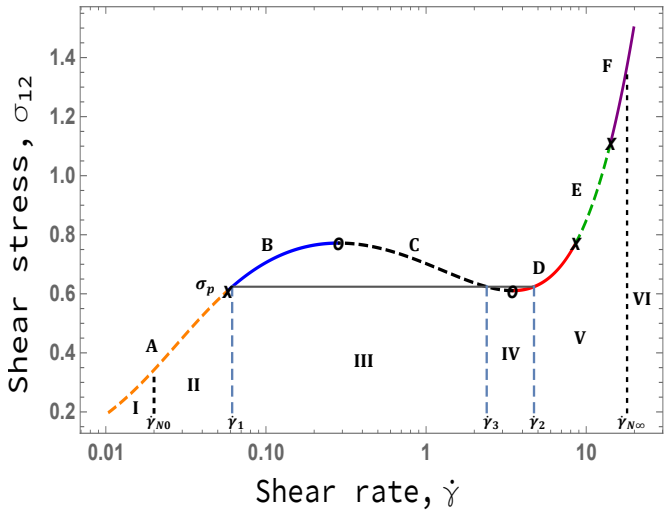

Figure 1: Simple shear flow curve predicted by the generalised BMP model. The parameters used are: $K_0\,\lambda = 0.09\,\mathrm{Pa}^{-1}\,\mathrm{s}$, $\varphi_0 = 0.05\,\mathrm{Pa}^{-1}\mathrm{s}^{-1}$, $\varphi_\infty = 13.5\,\mathrm{Pa}^{-1}\mathrm{s}^{-1}$, $G_0 = 0.38\,\mathrm{Pa}$ and $\vartheta = 0.8\,\mathrm{s}$.

2.2.1 Simple shear flow curve

Figure 1, 2 and 3 illustrate the behaviour of the viscometric functions, using as an example the following parameter values reported in [32, 13]: $K_0\,\lambda = 0.09\,\mathrm{Pa}^{-1}\,\mathrm{s}$, $\varphi_0 = 0.05\,\mathrm{Pa}^{-1}\mathrm{s}^{-1}$, $\varphi_\infty = 13.5\,\mathrm{Pa}^{-1}\mathrm{s}^{-1}$, $G_0 = 0.38\,\mathrm{Pa}$ and $\vartheta = 0.8\,\mathrm{s}$.

As shown in figure 1, the generalised BMP model predicts a non-monotonic behaviour for the shear stress against shear rate curve and it can be seen that there are characteristic regions of the curve that will be briefly explained in the following lines. Firstly, we have the line A, where the condition $H_0 > 0$ is satisfied. Within A, we find region I, for which a Newtonian-like behaviour (with viscosity $\eta = 1/\varphi_0$) is observed at very small shear rates. Thus, a low fluidity plateau $\varphi = \varphi_0$ is observed in the following range of shear rates:

$$\varphi \approx \varphi_0 \;\text{ when }\; \dot{\gamma}^2(1+\vartheta\dot{\gamma}) \ll \frac{\varphi_0}{K_0\,\lambda} \tag{15}$$

An increase in $\dot{\gamma}$ will lead to a shear-thinning behaviour (region II) until the fluid reaches a value of shear rate equal to $\dot{\gamma}_1$. The crosses marked in the plot represent *bifurcation* points that satisfy the equation $H_0 = 0$, where we have three real solutions for the fluidity but two of them are equal (depicted as circles).

Secondly, the points located in B, C and D correspond to the *multi-valued* region (where $H_0 < 0$), which is that region where the BMP model predicts that

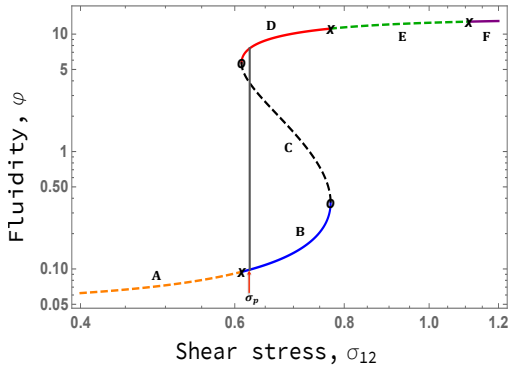

Figure 2: Fluidity vs shear stress calculated using equations (11) and (14). The parameter values used here are the same used in figure 1. The vertical line represents the location of the shear stress plateau σ_p and the crosses are the bifurcation points.

there are three possible values of shear-rate for a fixed value of shear stress. The most common example of this is the *shear stress plateau* σ_p and is represented here by the solid horizontal line. The vertical dashed lines indicate the location of its respective shear rate values, $\dot{\gamma}_1, \dot{\gamma}_2$ and $\dot{\gamma}_3$. The points of B located in region III, whose interval is $[\dot{\gamma}_1, \dot{\gamma}_3]$, are said to be meta-stable states, and the points that are also within region III and belong to C (characterised by a negative slope $\mathrm{d}\sigma_{12}/\mathrm{d}\dot{\gamma}$) are said to be mechanically unstable. Something similar is observed in region IV $[\dot{\gamma}_2, \dot{\gamma}_3]$, where there are also present unstable and meta-stable states (those to belong to D).

At higher values than $\dot{\gamma}_2$ (region V), the disentangled state (in which structure is being destroyed by flow) begins to take over. After the second bifurcation point, we have the region E ($H_0 > 0$), where the cubic equation predicts again a single real root. Finally, a third bifurcation point is predicted, and again three real solutions are obtained, but two of them are negative and just one is positive (plot line F). For values of shear rate higher than $\dot{\gamma}_\infty$ (region VI), we will observe a high fluidity plateau $\varphi = \varphi_\infty$, where the molecular networks have been completely destroyed. The condition that needs to be satisfied to observe region VI is the following:

$$\varphi \approx \varphi_\infty \;\text{ when }\; \dot{\gamma}^2(1 + \vartheta\dot{\gamma}) \gg \frac{\varphi_\infty}{K_0\,\lambda} \tag{16}$$

The shear-stress plateau σ_p (the point that satisfies the condition $R_0 = 0$) is one of the main characteristics of complex fluids that exhibit shear-banding, along with $\dot{\gamma}_1$ and $\dot{\gamma}_2$, known as *binodals* of the system. These three values are constantly observed and measured in experiments, and the reason for it is that when the fluid reaches the value of σ_p, there is a thermodynamically stable phase-coexistence between two bands of fluid that have different shear rates: the

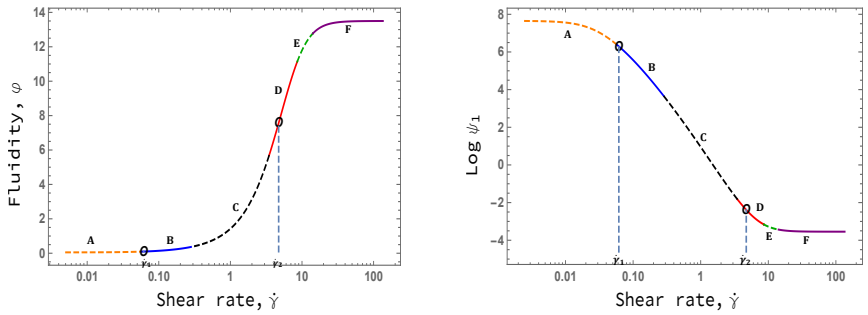

(a) Fluidity versus shear rate

(b) Ψ_1 versus shear rate

Figure 3: Fluidity and first normal stress difference coefficient versus shear rate. The parameter values used here are the same used in figure 1. The circles are the binodals of the system, $\dot{\gamma}_1$ and $\dot{\gamma}_2$.

entangled phase (where there exist branched networks) is seen for values smaller than $\dot{\gamma}_1$, and the disentangled phase (where there are polymer-like linear chains) appears at shear rates higher than $\dot{\gamma}_2$. The value $\dot{\gamma}_3$ is thermodynamically unfavourable and mechanically highly unstable. For a full detailed analysis of the flow curve, see [7].

2.2.2 Fluidity and first normal stress difference coefficient

In figure 2, we show the fluidity vs shear stress curve obtained in simple shear flow using the same parameter values as those used in figure 1. It can be clearly seen that for a fixed value of shear stress, there might exist multiple values of fluidity, such as the case of the stress *plateau* (solid vertical line). As indicated in figure 1, the crosses are the bifurcation points, and the small circles indicate the location of the minimum and the maximum seen in the simple shear flow curve. Outside the multi-valued zone, and at low shear stress (region A), we observe a low fluidity plateau with $\varphi \approx \varphi_0 = 0.05$, and similarly, $\varphi \to \varphi_\infty$ at high shear stress values (region F).

These fluidity plateaus can also be seen in the fluidity and first normal stress difference coefficient profiles, shown in figure 3. For both figures, the circles indicate the location of the binodals $\dot{\gamma}_1$ and $\dot{\gamma}_2$. The slope of these curves is much more pronounced than those seen in the equivalent model without shear-banding [9]. With an increase in shear rate, the fluid viscosity and elasticity drop.

2.3 Dimensionless form of the equations

2.3.1 Flow geometry

We now consider a two-dimensional channel flow of a fluid that satisfies the governing equations (constitutive equation (1)–(6) along with continuity and momentum equations (7)–(8)). Our channel has infinite extent in the x-direction and half-height L. The fluid is driven by a constant pressure gradient $\mathscr{P}$ in the x-direction, and flows with centreline velocity U_0. The flow geometry is sketched in figure 4.

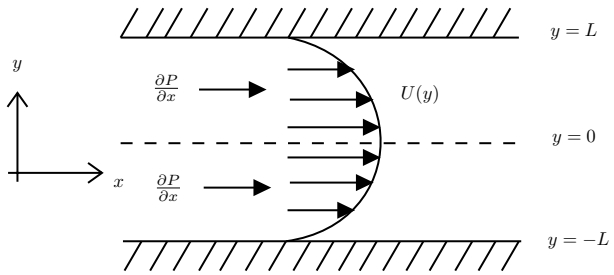

Figure 4: Flow geometry: two-dimensional pressure-driven channel flow or planar Poiseuille flow.

2.3.2 Dimensionless form of the governing equations

We scale lengths with L, times using the average shear rate U_0/L, and fluidities with the high-shear rate value φ_∞. The natural stress scale then becomes $\varphi_\infty^{-1}(U_0/L)$. In terms of dimensionless variables, the governing equations become:

$$\underline{\nabla} \cdot \underline{u} = 0 \tag{17}$$

$$Re\left(\frac{\partial \underline{u}}{\partial t} + \underline{u} \cdot \underline{\nabla} \underline{u}\right) = -\underline{\nabla} P + \underline{\nabla} \cdot \underline{\underline{\sigma}} \tag{18}$$

$$\underline{\underline{\sigma}} + \frac{W}{\varphi} \overset{\nabla}{\underline{\underline{\sigma}}} = \frac{2}{\varphi} \underline{\underline{D}} \tag{19}$$

$$\frac{D\varphi}{Dt} = \frac{1}{\Lambda}(\Phi - \varphi) + \Gamma\left(1 + \theta\sqrt{II_D}\right)(1-\varphi)\,\underline{\underline{\sigma}} : \underline{\underline{D}} \tag{20}$$

The dimensionless governing equations (17)–(19) obtained here are the same used in our previous work [9], where Re and W are the Reynolds and Weissenberg numbers, respectively, defined as:

$$Re = \rho\, U_0\, L\, \varphi_\infty \qquad W = \lambda_{ve}\left(\frac{U_0}{L}\right) = \frac{1}{G_0 \varphi_\infty}\left(\frac{U_0}{L}\right). \tag{21}$$

Equation (20) differs from the original Fredrickson's kinetic equation [19] by the shear-banding terms that appear in the right side of the equation. The other dimensionless numbers are:

$$\Phi = \frac{\varphi_0}{\varphi_\infty} \qquad \Lambda = \lambda\left(\frac{U_0}{L}\right) \qquad \Gamma = \left(\frac{1}{\varphi_\infty}\frac{U_0}{L}\right)K_0 \qquad \theta = \vartheta\left(\frac{U_0}{L}\right), \tag{22}$$

where Φ, Λ and Γ are the thixotropic ratio, the structural relaxation time and the destruction parameter, respectively, whose physical meaning will be discussed in the next subsection. We have introduced in this work, a new number, which is the *dimensionless shear-banding parameter* θ, defined as the ratio between ϑ and the characteristic time-scale of the flow. Its physical meaning is simple: for the cases where $\theta \to 0$, no phase coexistence is observed, and high values of θ will lead to the formation of bands with different shear rates. In the next sections, we will illustrate the effect of the shear-banding parameter on the rheology of the fluid

2.3.3 Generalised BMP model dimensionless numbers

In this section, we provide a brief explanation of the dimensionless numbers obtained above and other dimensionless groups that can be derived from (22). Firstly, the thixotropic ratio $\Phi = \varphi_0/\varphi_\infty = \eta_\infty/\eta_0$ is the ratio between zero and high shear rate fluidities, which indicates whether the fluid exhibits shear-thinning ($\Phi < 1$) or shear-thickening behaviour ($\Phi > 1$). A true yield stress will be observed if and only if $\Phi = 0$.

Secondly, we have the *structural relaxation* parameter or *thixoviscous* number Λ, which is defined as the ratio of the fluid's reformation time to a typical flow time. This number is one of a family of three dimensionless numbers introduced by Ewoldt & McKinley [14] to represent thixotropic elastoviscoplastic material responses: for high values of the thixoviscous number ($\Lambda \to \infty$), the fluid is said to be highly thixotropic; i.e. the fluid exhibits a slow or null recovery of viscosity after the cessation of flow; fast structural recovery or poorly thixotropic behaviour is seen for the opposite case ($\Lambda \to 0$). Another dimensionless number can be obtained if we combine Λ and the Weissenberg number, which is the *thixoelastic* number, $W_{te} = W/\Lambda$, defined as the ratio between the elastic relaxation time λ_{ve} and the structural relaxation time λ. This number is useful to distinguish viscoelastic effects from thixotropic ones.

The parameter associated with the breaking down of structure, Γ is defined as the ratio between K_0 and a characteristic stress value, $\varphi_\infty^{-1}(U_0/L)$. As described in [9], the parameter Γ will only appear in our steady equations in the combination $\Gamma\Lambda = \eta_\infty(U_0/L)^2/(K_0\lambda)^{-1}$, which is a relation between the viscous irreversible work and the kinetic structural work.

The previous parameters also helped us to define another highly important dimensionless number, the *thixoplastic number*, W_{tp}, defined as:

$$\lambda_{tp} = \frac{\eta_\infty}{\sigma_c} \qquad W_{tp} = \lambda_{tp}\left(\frac{U_0}{L}\right) = \sqrt{\Gamma\Lambda\,(1-2\Phi)}, \tag{23}$$

where $\sigma_c = (K_0\,\lambda\,\varphi_\infty[1-2\varphi_0/\varphi_\infty])^{-1/2}$ is the *critical shear stress* (the stress value that separates the regimes of *primary creep* and *accelerating flow* observed in fluids under the sudden startup of shear with imposed shear stress) and λ_{tp} is the plastic time-scale.

The thixoplastic number (which can also be seen as the inverse of the *Bingham* number) can provide us with the following information: for the case $W_{tp} = 0$, a true yield stress is seen; in the limit $W_{tp} \to 0$, an apparent yield stress is observed; and for higher values of W_{tp} the recovery of critical stress after flow is slow. We will use these dimensionless parameters throughout this paper to quantify our stability results.

3 Stability calculation

3.1 Base state

We study the stability of a TVEP fluid with shear-banding flowing through a two-dimensional channel flow of infinite extent in the x-direction, which has dimensionless height 2 (in the y-direction) and is being driven by a dimensionless constant pressure gradient $\mathcal{P}$ in the x-direction. Assuming a steady, unidirectional flow profile $\underline{u} = U(y)\underline{e}_x$ that satisfies a no-slip condition at $y = \pm 1$ (and denoting $U' = \mathrm{d}U/\mathrm{d}y$), equations (17)–(20) become:

$$0 = \mathcal{P} + \frac{\mathrm{d}\sigma_{12}}{\mathrm{d}y} \tag{24}$$

$$\sigma_{12} = \frac{1}{\varphi}\frac{\mathrm{d}U}{\mathrm{d}y} \qquad \varphi = \frac{\Phi + \Gamma\Lambda\big(1+\theta\,\dot{\gamma}\big)\sigma_{12}U'}{1+\Gamma\Lambda\big(1+\theta\,\dot{\gamma}\big)\sigma_{12}U'}. \tag{25}$$

Considering channel symmetry, the momentum equation (24) gives:

$$\sigma_{12} = -\mathcal{P}y. \tag{26}$$

Combining (26) into (25), we obtain a cubic equation for our dimensionless fluidity, whose coefficients are position-y dependent:

$$\varphi^3 + a\,\varphi^2 + b\,\varphi - c = 0 \tag{27}$$

$$a\,(y) = \frac{1}{\mathcal{P}y\,\theta} - 1 \qquad b\,(y) = \frac{1}{\Gamma\,\Lambda\,\theta\,\mathcal{P}^3y^3} - \frac{1}{\mathcal{P}y\,\theta} \qquad c\,(y) = \frac{\Phi}{\Gamma\,\Lambda\,\theta\,\mathcal{P}^3y^3}. \tag{28}$$

These equations are valid for $y > 0$, but may be extended to the whole channel by replacing y with $|y|$. We use Cardano's method to get an analytic solution

for the fluidity and some parameters that are useful to determine whether we will observe only one or more real solutions. These parameters have the same basic form as those for steady simple shear:

$$Q(y) = \frac{3b - a^2}{9} \qquad R(y) = \frac{9ab - 27c - 2a^3}{54} \qquad H(y) = Q^3 + R^2. \tag{29}$$

Using (26)–(29), we obtain a fluidity profile that resembles reported experimental information of shear-banding fluids, and is shown below:

$$\varphi(y) = \begin{cases} -\dfrac{1}{3}\,a + (S+T) & H(y) > 0 \\ 2\sqrt{-Q}\cos\left(\dfrac{\Theta}{3}\right) - \dfrac{1}{3}\,a & H(y) \le 0 \text{ and } R(y) \ge 0 \\ 2\sqrt{-Q}\cos\left(\dfrac{\Theta + 2\pi}{3}\right) - \dfrac{1}{3}\,a & H(y) \le 0 \text{ and } R(y) < 0, \end{cases} \tag{30}$$

where S, T and Θ are:

$$S(y) = \sqrt[3]{R + \sqrt{H}} \qquad T(y) = \sqrt[3]{R - \sqrt{H}} \qquad \Theta\,(y) = \cos^{-1}\left(\frac{R}{\sqrt{-Q^3}}\right). \tag{31}$$

The shear rate $\dot{\gamma}_0$ and the velocity profile $U(y)$ are simply calculated as follows:

$$\dot{\gamma}_0(y) = |U'| = \mathcal{P}\,y\,\varphi(y) \qquad U(y) = \int_0^1 \dot{\gamma}_0(y)\,\mathrm{d}y = \mathcal{P}\int_0^1 y\,\varphi(y)\,\mathrm{d}y \tag{32}$$

As it can be seen, an analytic equation for the velocity profile $U(y)$ of a fluid that exhibits shear-banding cannot be obtained (unlike the case without shear-banding, see equations (33)-(37) in [9]). Instead, we have to integrate $\dot{\gamma}_0(y)$ from the centreline to the channel wall. Additionally, the viscosity η and the stress tensor σ_{ij} are calculated as follows:

$$\eta = \varphi^{-1} = \frac{1 + \Gamma\Lambda\big(1 + \theta\,\dot{\gamma}\big)\sigma_{12}U'}{\Phi + \Gamma\Lambda\big(1 + \theta\,\dot{\gamma}\big)\sigma_{12}U'} \qquad \underline{\underline{\sigma}} = \begin{pmatrix} 2W\mathcal{P}^2y^2 & -\mathcal{P}y \\ -\mathcal{P}y & 0 \end{pmatrix}. \tag{33}$$

The first normal stress difference N_1 is simply:

$$N_1 = \sigma_{11} - \sigma_{22} = 2W\mathcal{P}^2y^2. \tag{34}$$

Lastly, the low ($\varphi = \Phi$) and high ($\varphi = 1$) dimensionless fluidity plateaus are seen when the following conditions are satisfied:

$$\varphi \approx \Phi \text{ when } \dot{\gamma}^2(1 + \theta\dot{\gamma}) \ll \frac{\Phi}{\Gamma\,\Lambda} \qquad \varphi \approx 1 \text{ when } \dot{\gamma}^2(1 + \theta\dot{\gamma}) \gg \frac{1}{\Gamma\,\Lambda} \tag{35}$$

In the next section, we will illustrate the behaviour of the fluidity, velocity and normal stress difference profiles predicted by the equations shown above.

3.2 Base state profiles

In this section, we show some of the velocity and fluidity profiles that can be obtained for various values of our model parameters. We begin with figure 5, where we illustrate characteristic base state profiles that are commonly observed in pressure-driven channel flow of fluids that exhibit shear-banding.

3.2.1 Base state profiles with shear banding

Firstly, in figure 5a) we have the velocity profile that was calculated from the integration of the shear rate profile (32). An extra calculation had to be done in order to satisfy the condition $U_0(0) = 1$: Newton-Raphson iterations are used to determine the required value of pressure gradient, which is $\mathcal{P} = 17.5927$ for this case.

As we can see, two regions can be identified in figure 5a): 1) a plug flow region of low fluidity (or high viscosity) that covers the channel from the centreline to a specific location close to the wall $y \approx \pm 0.8765$ and 2) a region near the wall ($|y| > 0.8765$) where the velocity drastically decreases towards its zero value at $y = \pm 1$. The regions are separated by an interface located at $y = \kappa = 0.8765$, where the high and low shear rate regions coexist. As stated above, the location of the interface can be simply obtained by requiring $R(\kappa) = 0$, which means that the location of the interface depends on our model parameters such as Γ, Λ, Φ and θ.

The resulting fluidity profile is shown in figure 5b). This time we will only show half the channel. For the low-shear-rate band, it can be seen that near the centreline $y \approx 0$ the fluidity has a value of $\varphi = \Phi = 0.001$. As we move along the channel, the fluidity exhibits some shear thinning behaviour, which leads to an increase in fluidity until the interface is reached, where there is a clear *jump* in the fluidity at $y = \kappa = 0.8765$ (see dotted lines and circles). The second band with a much lower viscosity than the first one appears, and its viscosity will increase until the channel wall is reached. The shear rate profile $\dot{\gamma}$ vs y looks qualitatively very similar to the fluidity one, so we will not show it here.

A particularity of the BMP model (compared to other viscoelastic models) is that there is continuity at the interface in the first normal stress difference for fluids that exhibit shear-banding, as can be seen in figure 5c) (see black circle), which shows a parabolic profile for N_1 as a function of the channel coordinate. The discontinuity that we saw for Ψ_1 in section 2.2 is due to the jump in shear rate, or equivalently to a jump in fluidity.

The last figure is 5d), which illustrates the flow curve for pressure-driven channel flow of our fluid, where we show the only physically-possible dynamic states of the system (unlike figure 1 that shows metastable and unstable regions). The interface appears when the flow reaches a shear stress plateau value of $\sigma_p = 15.42$ (see horizontal dashed line), which will lead to a band of fluid with

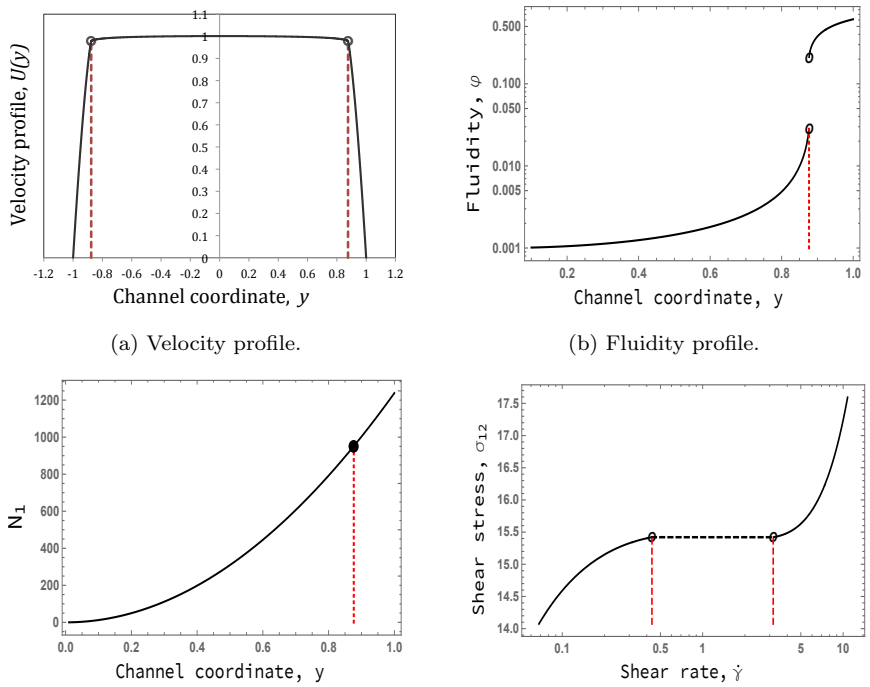

(a) Velocity profile.

(b) Fluidity profile.

(c) First normal stress difference.

(d) Flow curve.

Figure 5: Velocity, fluidity and first normal stress difference profiles and flow curve calculated using equations (27)–(34) with $\Phi = 0.001$, $\Gamma\Lambda = 0.004$, $W = 2$ and $\theta = 0.10$. For all the panels, the vertical dotted lines represent the location of the interface κ between the low and high shear rate bands and the circles are the binodals of the system and their respective value of velocity (a), fluidity (b), $N1$ (c), and shear stress plateau between the two values of shear rate which meet at $y = \kappa$ (d).

$\dot{\gamma}_1 = 0.4353$ and another one with $\dot{\gamma}_2 = 3.1785$ at $y = \kappa = 0.8765$.

Lastly, an important flow condition that needs to be satisfied in order to see shear-banding within the channel (even though the shear-banding parameter has a non-zero value), is that the wall shear stress σ_w has to be greater than the stress plateau σ_p (for this case, $\sigma_w = 17.59 > \sigma_p$), otherwise, the low shear rate band will fill the whole channel.

3.2.2 Transition to shear-banding

In this section, we will show the effect of the dimensional shear-banding parameter θ on the base state quantities in pressure-driven channel flow of our fluid. We choose fixed values of $\Phi = 0.001$ and $\Gamma\Lambda = 0.004$ and a set of values of

$\theta = [0, 0.05, 0.08, 0.1, 1, 3, 10]$ to illustrate the transition from non-shear banding to the formation of bands. The results can be seen in figure 6.

Firstly, we focus on small values of θ. We show the velocity profiles predicted by our equations in figure 6a), where the bottom curve depicts the case for a fluid with a value of $\theta = 0$, with a plug-flow along the channel commonly observed in shear-thinning fluids. An increase in the shear-banding parameter (from bottom to top) slowly leads to a wider high viscosity region near the channel wall, until an interface between two bands of fluid with different shear rates is seen at $y = \kappa \approx 0.8765$ (case $\theta = 0.1$).

This transition can be better appreciated in the fluidity profile across the channel, see figure 6c). For the case $\theta = 0$, we observe a continuous increase of the fluidity from the centreline towards the channel-wall. Although the same behaviour is observed for the cases $\theta = 0.05$ and $\theta = 0.08$, notice how the slope of the curves increases (rapid increase in φ between $y = 0.7$ and $y = 0.9$), until we observe a discontinuity in the curve φ vs y, indicating that two bands of fluid with different viscosities have been formed. The jump in the fluidity value is represented with a dashed line when $\theta = 0.10$.

The transition from monotonic to non-monotonic flow curves can be seen in figure 6e). Notice how an increase in θ leads to a stress plateau σ_p, with two representative binodals: $\dot{\gamma}_1$ at low shear rates and $\dot{\gamma}_2$ at high shear rates.

For the cases with high shear-banding parameter values, the flow behaviour is similar to the one reported with $\theta = 0.1$. However, there are gradual changes; for instance, we have the velocity profiles in figure 6b). From right to left, the values are $\theta = 0.3, 1, 3$ and 10. For all cases, there exists an interface that separates the low viscosity band from the high one (see vertical dashed lines), but we can see that an increase in the shear-banding parameter moves the location of the interface, κ, away from the channel wall. This is consistent with the flow curves shown in 6f), where the stress plateau σ_p, and the binodals $\dot{\gamma}_1$ and $\dot{\gamma}_2$ shift to lower values as θ grows.

The fluidity profiles 6d) are also in agreement with the velocity profiles. We observe that a rise in the shear-banding parameter value causes the jump in the fluidity curves to increase for large θ. The limit will be when the fluidity in the low region φ_1 is equal to the thixotropic ratio Φ (fully entangled state), and the high region fluidity φ_2 reaches a value of 1 (fully destroyed state). As we will see in the next section, how quick or slow the transition from non-shear-banding to shear-banding is will depend on the values of the destruction parameter Γ, thixoviscous number Λ and thixotropic ratio Φ.

3.2.3 Dependence of transition on destruction parameter and thixoviscous number

In this section, we focus on fixed values of the thixotropic ratio $\Phi = 0.001$ and shear-banding parameter $\theta = 0.1$ to study the effect of a variable product $\Gamma\Lambda$

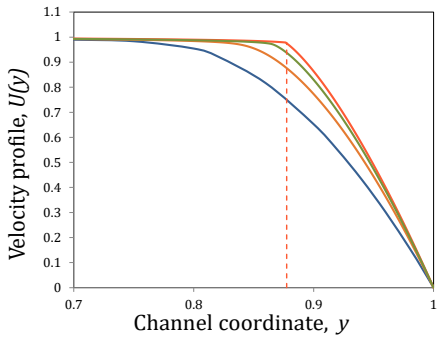

(a) Velocity profile with small θ.

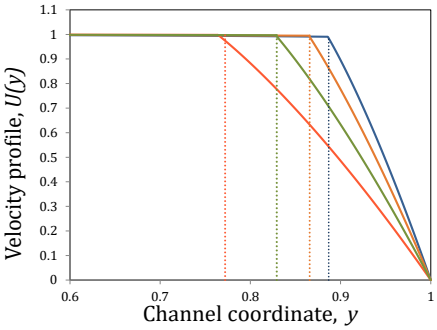

(b) Velocity profile with high θ.

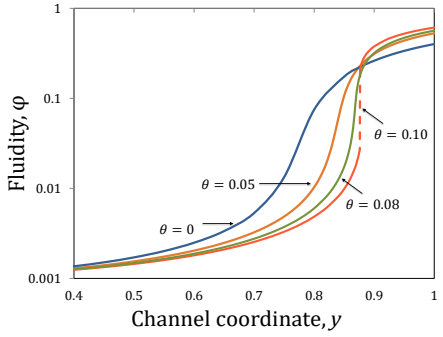

(c) Fluidity profile with small θ.

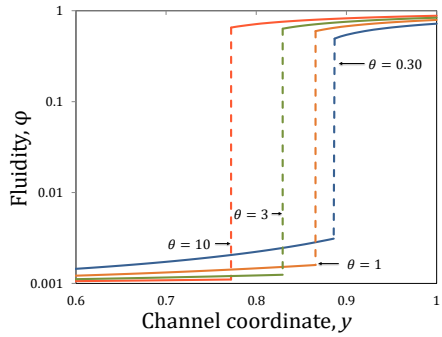

(d) Fluidity profile with high θ.

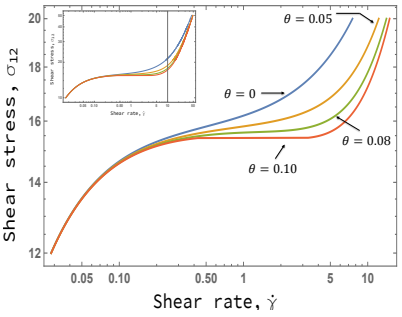

(e) Flow curve with small θ.

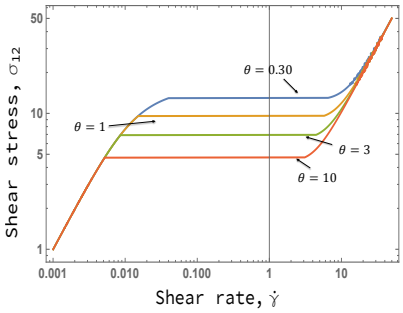

(f) Flow curve with high θ.

Figure 6: Base state profiles for different values of shear-banding parameter, with $\Phi = 0.001$ and $\Gamma\Lambda = 0.004$ fixed. Figure (a) velocity profile for small θ values; from bottom to top $\theta = 0, 0.05, 0.08$ and 0.1. Figure (b) velocity profile for high θ values; from top to bottom $\theta = 0.3, 1, 3$ and 10. The vertical dashed lines represent the location of the interface κ. Figures (c) and (d) are the fluidity profiles for low and high θ values , and finally, figures (e) and (f) show their respective flow curves σ_{12} vs $\dot{\gamma}$.

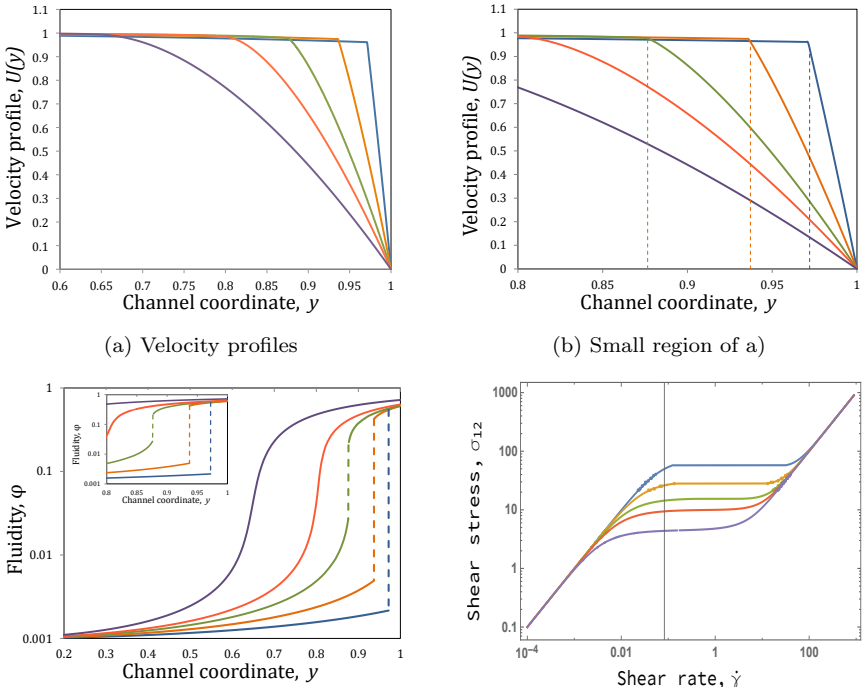

(a) Velocity profiles

(b) Small region of a)

(c) Fluidity profiles

(d) Flow curve σ_{12} vs $\dot{\gamma}$

Figure 7: Base state profiles for different values of $\Gamma\Lambda$, with $\Phi = 0.001$ and $\theta = 0.10$ fixed. Figure (a) Velocity profile; from right to left: $\Gamma\Lambda$=$1.6 \times 10^{-4}, 0.001, 0.004, 0.01$ and 0.05. Figure (b): small region of figure (a). The dashed lines here indicate the location of the shear-banding interface κ. (c) Fluidity profiles; from left to right, the shear-banding parameter is increasing, with the same parameter values indicated above. The dashed lines represent the discontinuity (or jump) in the fluidity values. Figure (d): flow curve for the same parameters used in (a); from top to bottom, $\Gamma\Lambda$ increases.

on the formation of shear bands. As we previously explained, the destruction parameter Γ and the structural reformation parameter Λ will only affect the base state quantities through their product (this will not be true for the flow instability, as we will show in the next sections). Small values of $\Gamma\Lambda$ involve slow destruction (or equivalently, quick structural reformation), while high structural destruction or high thixotropy will be observed for large values of $\Gamma\Lambda$. In order to explore these structural changes in our fluids, we choose a set of values of $\Gamma\Lambda = [1.6 \times 10^{-4}, 0.001, 0.004, 0.01, 0.05]$. Results are shown in figure 7.

Figure 7a) illustrates the velocity profiles for different values of the product $\Gamma\Lambda$. For the limit $\Gamma\Lambda \approx 0$, no jump in fluidity is reported, as the interface location would appear outside the channel. The smallest value of $\Gamma\Lambda$ here is 1.6×10^{-4}, whose curve is located farthest to the right of the plot. We can see

for this case that a plug-flow is almost all over the channel, with an interface located very close to the channel wall ($y \approx 0.973$) and with an extremely narrow high-fluidity region. These observations can be seen more clearly in figure 7b), which is a *zoom* of the bigger figure. As we increase the value of $\Gamma\Lambda$ (from right to left), the interface location κ (vertical dashed line) moves away from the channel wall, meaning that the low-viscosity band becomes wider and the plug-flow occupies less of the flow width.

The fluidity profiles shown in figure 7c) are useful to appreciate the transition better. For instance, we can clearly see that an increase in $\Gamma\Lambda$ (i.e. a rise in structural destruction and/or thixotropy of the fluid) is increasing the high-shear rate band width and reducing the *jump* in the fluidity curves, until a *critical* value of $\Gamma\Lambda \approx 0.0045$ is reached, which is where the interface disappears, or in other words, the fluidity profiles are no longer discontinuous. For $\Gamma\Lambda > 0.0045$, the fluidity profiles will always be continuous (but with a high slope) and the high-shear rate band will get wider and wider. It is important to point out that this critical value of $\Gamma\Lambda \approx 0.0045$ is only valid for $\theta = 0.1$ and $\Phi = 0.001$, and therefore, the formation of the bands will depend on these parameters.

We also show the flow curves 7d), where we observe that an increase in $\Gamma\Lambda$ (from top to bottom) decreases the values of the shear stress plateau σ_p and binodals $\dot{\gamma}_1$ and $\dot{\gamma}_2$, until we no longer see a plateau (two bottom curves).

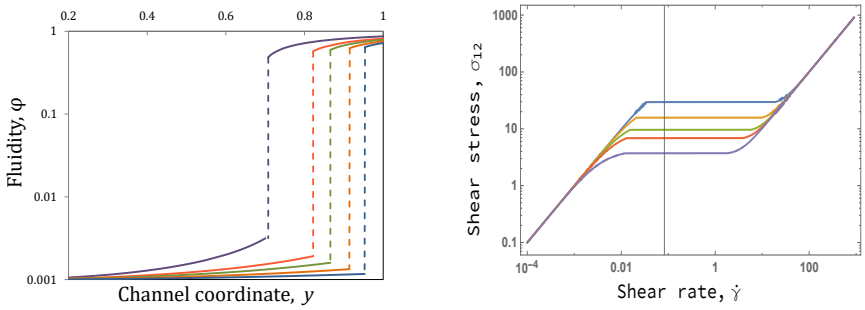

(a) Fluidity profiles

(b) Flow curve σ_{12} vs $\dot{\gamma}$

Figure 8: Fluidity profiles and flow curves for different values of $\Gamma\Lambda$, with $\Phi = 0.001$ and $\theta = 1.0$ fixed. Figure (a) Fluidity profile; from right to left: $\Gamma\Lambda$=$1.6 \times 10^{-4}, 0.001, 0.004, 0.01$ and 0.05. The dashed lines represent the discontinuity (or jump) in the fluidity values at κ. Figure (b): flow curves); from top to bottom, $\Gamma\Lambda$ increases.

Finally, in figure 8 ,we explore the behaviour of the fluidity profiles and the flow curves with $\Gamma\Lambda$ variable but this time for a much higher value of shear-banding parameter, $\theta = 1.0$. The rest of the parameters are the same as the ones used in figure 7. In contrast with the fluidity profiles reported in 7c), where continuity is seen for high values of $\Gamma\Lambda$, notice that when $\theta = 1.0$, a jump is still observed, as seen in figure 8a). Additionally, for the curve with the lowest

$\Gamma\Lambda = 1.6 \times 10^{-4}$, the low-fluidity plateau $\varphi = \Phi = 0.001$ covers most of the channel, until it *jumps* to a much higher fluidity near the wall. This is also evident in its flow curve shown in figure 8b), which is located at the top. For these parameter values (low $\Gamma\Lambda$ and high shear-banding parameter), we see that the high-viscosity region is approximately Newtonian right up to the banding interface: that is, the shear-thinning region II described in section 2.2.1 has been eliminated.

3.3 Perturbation flow

We add an infinitesimal perturbation ε to the base flow, modifying all quantities by a small change :

$$\underline{u} = (U + u\varepsilon, v\varepsilon) \tag{36}$$

$$\underline{\underline{\sigma}}^{tot} = \underline{\underline{\sigma}} + \varepsilon\underline{\underline{\Sigma}} \qquad \underline{\underline{\sigma}}^{tot} = \begin{pmatrix} \sigma_{11} + \Sigma_{11}\varepsilon & \sigma_{12} + \Sigma_{12}\varepsilon \\ \sigma_{21} + \Sigma_{21}\varepsilon & \sigma_{22} + \Sigma_{22}\varepsilon \end{pmatrix} \tag{37}$$

$$\varphi_p = \varphi + \phi\varepsilon \tag{38}$$

$$\underline{\underline{D}} = \underline{\underline{D}}_0 + \underline{\underline{d}}\varepsilon, \tag{39}$$

$$\dot{\gamma} = \dot{\gamma}_0 + \dot{\gamma}_p\varepsilon, \tag{40}$$

$$P_p = P_0 + \varepsilon p, \tag{41}$$

in which all the perturbation quantities are functions of the channel coordinate y, and ε represents a single Fourier mode:

$$\varepsilon = \epsilon \exp\left[\mathrm{i}kx - \mathrm{i}\omega t\right]. \tag{42}$$

Denoting D as differentiation with respect to y, the continuity equation becomes:

$$\mathrm{i}ku + \mathrm{D}v = 0. \tag{43}$$

We now introduce the streamfunction ψ to reduce one dependent variable, defined as:

$$u = \mathrm{D}\psi \qquad v = -\mathrm{i}k\psi, \tag{44}$$

which automatically satisfies the continuity equation. Discarding terms of order ϵ^2, the remaining governing equations become:

$$Re(-\mathrm{i}\omega\mathrm{D}\psi - \mathrm{i}k\psi\mathrm{D}U + \mathrm{i}kU\mathrm{D}\psi) = -\mathrm{i}kp + \mathrm{i}k\Sigma_{11} + \mathrm{D}\Sigma_{12} \tag{45}$$

$$Re(-k\omega\psi + k^2U\psi) = -\mathrm{D}\,p + \mathrm{i}k\Sigma_{12} + \mathrm{D}\Sigma_{22} \tag{46}$$

$$\phi = \frac{\Gamma(1-\varphi)(1+\theta\dot{\gamma}_0)\left[\mathrm{i}k\sigma_{11}\mathrm{D}\psi + \sigma_{12}(\mathrm{D}^2+k^2)\psi + \Sigma_{12}\mathrm{D}U\right] + \mathrm{i}k\psi\mathrm{D}\varphi}{\left[-\mathrm{i}\omega + \mathrm{i}kU + \Lambda^{-1} + \Gamma\sigma_{12}\mathrm{D}U(1+\theta\dot{\gamma}_0)\right]} + \frac{\Gamma\sigma_{12}\mathrm{D}U(1-\varphi)\theta\dot{\gamma}_p}{\left[-\mathrm{i}\omega + \mathrm{i}kU + \Lambda^{-1} + \Gamma\sigma_{12}\mathrm{D}U(1+\theta\dot{\gamma}_0)\right]} \tag{47}$$

$$\Sigma_{22}(-\mathrm{i}\omega W\eta + \mathrm{i}kUW\eta + 1) = 2\eta(W\sigma_{12}k^2\psi - \mathrm{i}k\mathrm{D}\psi) \quad (48)$$

$$\Sigma_{12}(-\mathrm{i}\omega W\eta + \mathrm{i}kUW\eta + 1) = \eta(\mathrm{D}^2 + k^2)\psi - \xi\mathrm{D}U + \mathrm{i}k\psi W\eta\mathrm{D}\sigma_{12} + W\eta(\sigma_{11}k^2\psi + \Sigma_{22}\mathrm{D}U) \quad (49)$$

$$\Sigma_{11}(-\mathrm{i}\omega W\eta + \mathrm{i}kUW\eta + 1) = 2\eta\mathrm{i}k\mathrm{D}\psi - 2W\xi\sigma_{12}\mathrm{D}U + \mathrm{i}k\psi W\eta\mathrm{D}\sigma_{11} + 2W\eta(\mathrm{i}k\sigma_{11}\mathrm{D}\psi + \sigma_{12}\mathrm{D}^2\psi + \Sigma_{12}\mathrm{D}U) \quad (50)$$

in which ξ and $\dot{\gamma}_p$ are :

$$\xi = \frac{\phi}{\varphi^2} \qquad \dot{\gamma}_p = -\left(\mathrm{D}^2\psi + k^2\psi\right) \quad (51)$$

and the base state quantities η and σ_{ij} are:

$$\eta = \varphi^{-1} = \frac{1 + \Gamma\Lambda\big(1 + \theta\,\dot{\gamma}\big)\sigma_{12}\mathrm{D}U}{\Phi + \Gamma\Lambda\big(1 + \theta\,\dot{\gamma}\big)\sigma_{12}\mathrm{D}U} \qquad \underline{\underline{\sigma}} = \begin{pmatrix} 2W\mathcal{P}^2y^2 & -\mathcal{P}y \\ -\mathcal{P}y & 0 \end{pmatrix}. \quad (52)$$

3.4 Boundary conditions

The coupled system of equations (45)–(52) can be combined and the resulting equation is a fourth-order ODE in ψ dependent on y. The boundary conditions are conditions of no flow on the boundaries:

$$\psi = \mathrm{D}\psi = 0 \text{ at } y = \pm 1. \quad (53)$$

This system is governed by seven dimensionless parameters: the Reynolds Re and Weissenberg W numbers, the wavenumber k, the thixotropic ratio Φ, the shear-banding parameter θ and the reformation/destruction parameters Λ and Γ. For fixed values of the parameters mentioned above, we look for the frequency or *eigenvalue* of the system, ω; more specifically, its imaginary part or *growth rate*, $\Im(\omega)$ to deduce whether a flow is stable or not: for $\Im(\omega) > 0$, the flow is said to be unstable as the perturbations grow with time. The opposite is seen when $\Im(\omega) < 0$.

3.4.1 Continuity in the fluidity profile

Although the shear-banding parameter θ had a non-zero value, that would not necessarily mean we will observe shear bands (or a jump in the viscosity). Instead, at some parameter values, we will see a continuous fluidity profile, as we previously analysed in sections 3.2.2 and 3.2.3. For these cases, the numerical method is simple and is the same we used in [8, 9]: we solve the ODE using the shooting method of Ho & Denn [23], which consists of integrating the governing equations from the centreline to the channel wall, until we find the correct eigenvalue $\Im(\omega)$ that satisfies the boundary conditions at the wall $y = \pm 1$ and the ones at the centreline.

The boundary conditions at $y = 0$ (considering appropriate symmetry) will depend on the kind of mode that is perturbing the flow; a) varicose modes, for which ψ is an odd function of y and b) sinuous modes, for which ψ is an even function of y:

$$\psi = \mathrm{D}^2\psi = 0 \text{ at } y = 0 \qquad \text{for varicose modes,} \tag{54}$$

$$\mathrm{D}\psi = \mathrm{D}^3\psi = 0 \text{ at } y = 0 \qquad \text{for sinuous modes.} \tag{55}$$

We use as initial estimates the results obtained in [9] to make parameter continuation in θ, until we observe a jump in fluidity, for which we use the method described below.

3.4.2 Shear-band flow

The numerical method drastically changes when there is a discontinuity in the fluidity profiles, which leads to the formation of shear bands, whose interface in the base state is located at $y = \kappa$. As we have previously explained, the location of the interface along the channel depends on our flow parameters $\kappa = \kappa\,(\Gamma, \Lambda, \Phi, \theta)$, and its numerical value is found when we satisfy the following equation:

$$R(\kappa) = 0, \tag{56}$$

where R, see equation (29), is an expression that depends on the coefficients of the cubic equation for the fluidity (27). When a perturbation is imposed to the base state flow, there will be an infinitesimal displacement ζ of a fluid particle located in the interface, which leads to a kinematic boundary condition, in which the interface is defined by $y = \overline{\eta} + \zeta\varepsilon$, where $\overline{\eta}$ is a Lagrangian coordinate that satisfies:

$$\frac{D\,\overline{\eta}}{Dt} = \frac{\partial \overline{\eta}}{\partial t} + \underline{u} \cdot \underline{\nabla}\,\overline{\eta} = 0. \tag{57}$$

The physical meaning of equation (57) is that there is no mass transport through the interface, and therefore, fluid particles on the interface always remain part of the interface. Moreover, equation (57) is a common boundary condition used when there is an interface separating two different fluids, but it has also been applied to shear-banded flows [39, 38]. For our linear stability analysis problem, if our interface initially located at $\overline{\eta} = \kappa$ is displaced from $y = \kappa$ to $y = \overline{\eta} + \zeta\varepsilon$, and if ζ is small, the kinematic boundary condition (after correcting to linear order terms) becomes:

$$-\mathrm{i}k\psi - (-\mathrm{i}\,\omega + \mathrm{i}kU)\zeta = 0. \tag{58}$$

Furthermore, we require continuity across the interface of the velocity components $U + \underline{u}$ and of the traction (force balance at the interface), $\left(\underline{\underline{\sigma}} + \varepsilon\underline{\underline{\Sigma}}\right) \cdot \underline{n}$ (where $\underline{n}$ is the normal to the interface); this requires:

$$[\psi] = 0 \qquad [\mathrm{D}\psi + \zeta\,\mathrm{D}U] = 0 \tag{59}$$

$$[\Sigma_{12}] = 0 \qquad [\mathrm{D}\Sigma_{12} + \mathrm{i}k(\Sigma_{11} - \Sigma_{22})] = 0, \tag{60}$$

where we use $[x]$ to denote the jump in quantity x across the interface $y = \kappa$. In order to solve our stability problem, we integrate the governing equations (45)–(51) using the shooting method [23] from the centreline (with boundary conditions for either varicose (54) or sinuous modes (55)) to the interface, and from the channel wall (with non-slip boundary conditions (53)) to the interface. The four jump conditions (59)–(60) at the interface $y = \kappa$ then become a matrix equation of the form:

$$M\Psi = 0, \tag{61}$$

where Ψ is the vector of coefficients of each of the four linearly independent basic functions. Thus, the true solution of the system is found when the determinant of $M(\omega)$ is zero. A Newton-Raphson technique is used to find a zero of the determinant as a function of ω, as in the case without interface.

4 Results

4.1 Shear-banding parameter variable

In our previous work [9], we studied the isolated and combined effect of the BMP model parameters on the flow instability, and we identified under which conditions it is likely to observe highly unstable flows. Here we will carry out similar calculations and explain the results, but we will begin by varying the new dimensionless number that appears in this work: the shear-banding parameter.

In order to illustrate the effects of θ, we simply choose and fix values of destruction parameter, thixoviscous number, wavenumber, Reynolds and Weissenberg numbers and thixotropic ratio. For the last three cases, we will use a fixed value for almost all the calculations throughout the paper. For the Reynolds number, we set $Re = 0$ because we are interested in studying elastic instabilities rather than inertial ones. For the Weissenberg number, we will be using $W = 2$, as we know that an increase in W was destabilising for the modes seen in our previous work [9] (we will show that this is also the case for TVEP fluids that exhibit shear-banding). And lastly, although it is not numerically possible for us to explore the case of a fluid with a true yield stress ($\Phi = 0$), unstable flows are seen when there is a decrease in Φ, so we will fix $\Phi = 0.001$, as this is one of the values that we previously reported where strong instabilities happen. In the subsections below we will show and analyse the results obtained.

4.1.1 Critical shear-banding parameter value

In this section, we make parameter continuation in θ, and choose as our initial values base states that are found to be unstable in the absence of shear-banding ($\theta = 0$). We select two different values of the destruction parameter: $\Gamma = 0.003$

and $\Gamma = 0.005$. We set $W = 2$, $\Lambda = 1$, $\Phi = 0.001$ and $k = 0.1$. The results for sinuous perturbations are shown in figure 9.

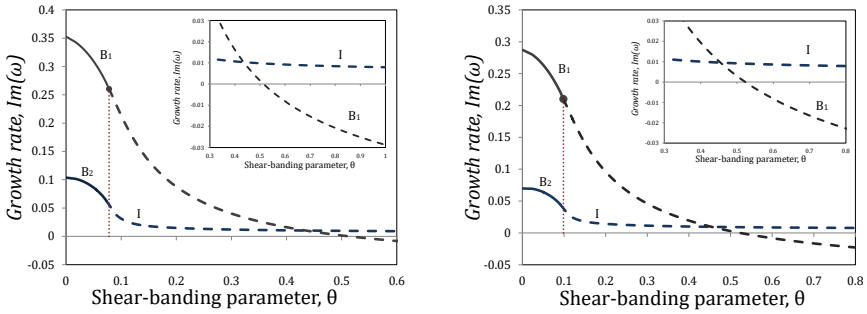

(a) $\Gamma\Lambda = 0.003$ (b) $\Gamma\Lambda = 0.005$

Figure 9: Growth rate against shear-banding parameter θ for sinuous modes, with $W = 2$, $\Lambda = 1$, $\Phi = 0.001$ and $k = 0.1$ fixed. Inertia is neglected ($Re = 0$). Figure (a): $\Gamma = 0.003$; (b): $\Gamma = 0.005$. For both pictures: the solid lines represent base-states without bands; dashed lines indicate that there are bands of fluids with a jump in the fluidity profile; the dotted line shows the location of the critical value of θ.

We can see for both cases that at low values of θ, there are two modes, B_1 and B_2, which we call *bulk* modes (this definition is explained in section 4.1.2). It can be seen that the mode B_1 (which is the kind of mode we studied in our previous work [9]) is always more unstable than the mode B_2. We then increase the values of the shear-banding parameter, and we observe that there is a decrease in the growth rate for both cases. By increasing θ, the slope of the fluidity profiles in the channel is increasing rapidly (as in sections 3.2.2 and 3.2.3), which means that the fluid is beginning to separate into two bands. Continuity in the fluidity profiles is seen for all the points that are plotted with the solid line. The *jump* in the viscosity (characteristic in shear-banded flows) is first seen at a critical value of $\theta_c \approx 0.078$ for $\Gamma = 0.003$ and $\theta_c \approx 0.0985$ for $\Gamma = 0.005$. These points are indicated in their respective plots with black circles. After these critical values, we observe pure shear-banding fluids (all the points that are in the dashed lines), which become less and less unstable as we increase θ, indicating that a reduction in the value of the stress plateau and its binodals $\dot{\gamma}_1$ and $\dot{\gamma}_2$ reduces the growth rate of instability. The mode B_1 in both cases eventually reach stability for high values of the shear-banding parameter, and this happens approximately when $\theta \approx 0.515$ for $\Gamma = 0.003$ and $\theta \approx 0.522$ for $\Gamma = 0.005$.

More interestingly, above the critical shear-banding parameter value, the mode B_2 becomes an *interfacial* mode (the reason for this name is explained in section 4.1.2). This mode (which is shown in the figures as "I") appears when there is an interface that separates the bands with different shear rates, and this

is seen when there is a jump in the fluidity. Although the mode I also becomes less unstable as we increase θ, the decay of the growth rate of this mode is extremely slow compared to the other mode B_1, and above a given value of θ, the interfacial mode now will be more unstable than the bulk one (see small figures in 9).

We have determined that these interfacial modes will be dominant when the binodal $\dot{\gamma}_1$ (i.e. the low dimensionless shear rate value that corresponds to one of the bands formed when the system reaches the stress plateau σ_p, see section 3.2.2), obeys the condition established in (35):

$$\dot{\gamma}_1^2(1+\theta\dot{\gamma}_1) \ll \frac{\Phi}{\Gamma\Lambda}. \tag{62}$$

Physically, this means that the shear-thinning behaviour (region II in the flow curve, see figure 1) will vanish, and therefore, the fluidity of the low band would be approximately equal to the value of the thixotropic ratio Φ (see figure 6d). The condition (62) is satisfied at high values of the shear-banding parameter θ, which will lead to dominant interfacial instabilities rather than bulk ones, where the shear-thinning characteristics are key components, as shown in our previous works. The bulk modes, as we have seen, dominate over the interfacial ones at values of θ slightly above the critical shear-banding parameter value θ_c.

4.1.2 Dispersion relations: bulk and interfacial modes

The generalised BMP model is able to predict two kinds of modes: bulk and interfacial modes. Two bulk modes were found in the non-shear-banding region, B_1 and B_2, being B_1 the more unstable one. In addition, B_1 is found to still be present in the shear-banding region. On the other hand, the bulk mode B_2 becomes an interfacial mode "I" at values of θ above the critical shear-banding parameter value θ_c (when there appears a jump in the fluidity). In a recently published paper [38], Renardy *et al.* studied stability analysis of two-dimensional plane Couette flow of viscoelastic fluids with thixotropic yield stress behaviour and shear-banding and they found similar results to ours: *bulk* instabilities in the yielded phase, and for some given values of their model parameters, they also observed unstable *interfacial* instabilities. The main difference with respect to our case is that the interfacial modes they reported are driven by a jump in the normal stress difference across the interface

A key contributions of their paper is that they establish a criterion that allows us to distinguish between *bulk* and *interfacial* modes: the *interfacial* modes are neutrally stable as $k \to 0$. In this way, we compare the interfacial and bulk modes obtained in figure 9 by taking one point of each mode that is within the shear-banding region (dashed lines), and we vary the wavenumber k to study their behaviour. Results can be seen in figure 10.

We set a constant low value of shear-banding parameter $\theta = 0.1180$, which ensures that bands of fluid are formed in the base state, and therefore, two

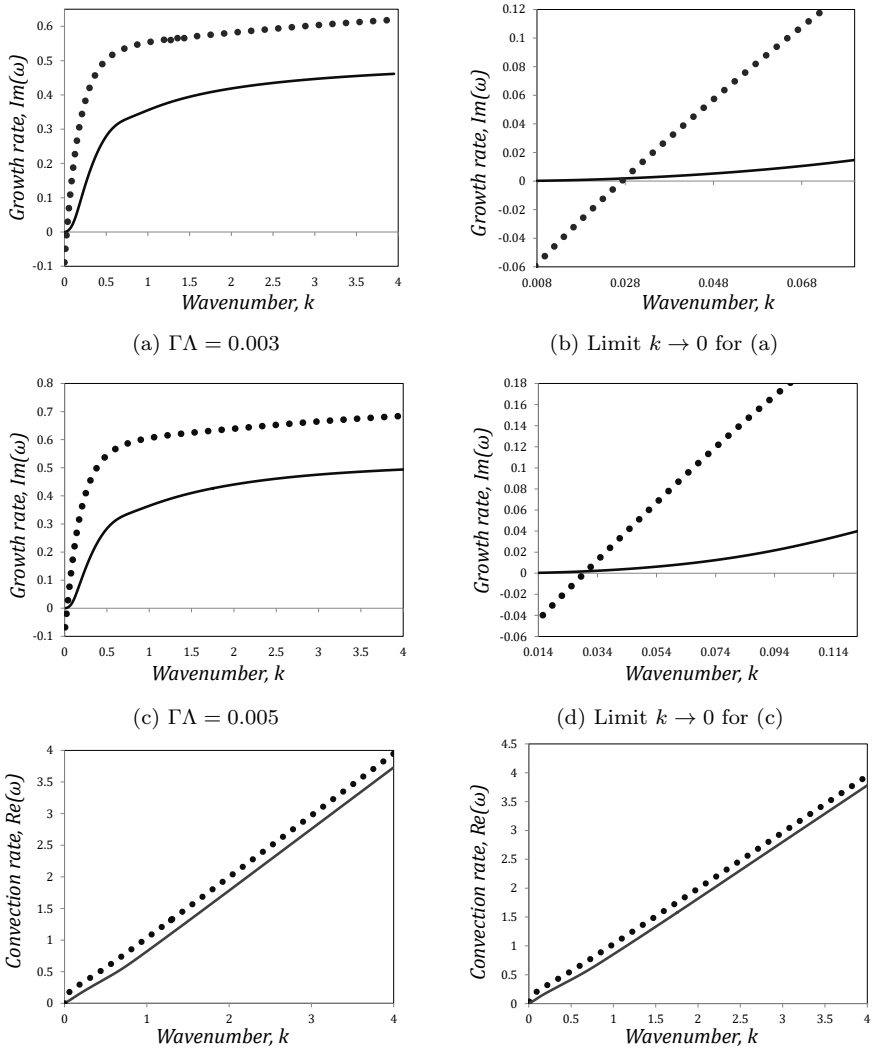

(a) $\Gamma\Lambda = 0.003$

(b) Limit $k \to 0$ for (a)

(c) $\Gamma\Lambda = 0.005$

(d) Limit $k \to 0$ for (c)

(e) $\Re(\omega)$ vs k for $\Gamma\Lambda = 0.003$

(f) $\Re(\omega)$ vs k for $\Gamma\Lambda = 0.005$

Figure 10: Dispersion relations $\Im(\omega)$ vs k for bulk (dotted lines) and interfacial (solid lines) modes, with $\theta = 0.1180$, $W = 2$, $\Lambda = 1$ and $\Phi = 0.001$ fixed. The plots are for sinuous modes. Figure (a), (b) and (e) show the case for $\Gamma = 0.003$, while (c), (d) and (f) are for $\Gamma = 0.005$.

modes of instability are present, B_1 and I, according to what we saw in figure 9. Parameter continuation for the cases $\Gamma\Lambda = 0.003$ and $\Gamma\Lambda = 0.005$ is made for the wavenumber k. For both cases, both modes tend to be more unstable for short waves, reaching an asymptotic value for $k > 1.0$. However, there are remarkable differences between the two modes: one of them, the bulk mode

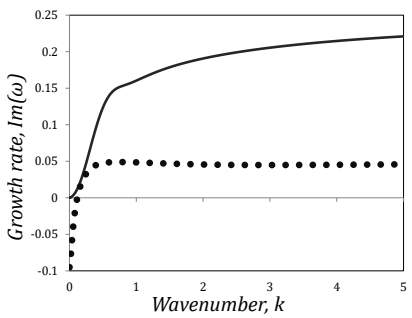

(a) $\Im(\omega)$ vs k

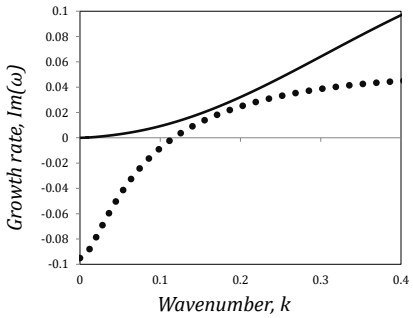

(b) $\Im(\omega)$ vs k: long waves $k \to 0$

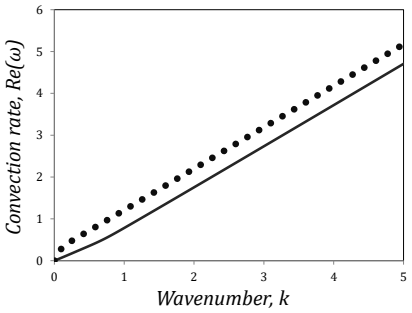

(c) $\Re(\omega)$ vs k

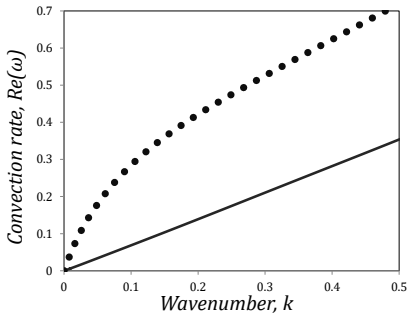

(d) $\Re(\omega)$ vs k: long waves $k \to 0$

Figure 11: Dispersion relations for both sinuous bulk and sinuous interfacial modes with $W = 2$, $\Lambda = 1$, $\Gamma = 0.003$, $\theta = 0.60$ and $\Phi = 0.001$ fixed. For all plots, the solid line depicts the interfacial modes. Figure (a): growth rate against wavenumber. Figure (c): convection rate against wavenumber.

(dotted lines) is always a lot more unstable than the interfacial one (solid lines), but more importantly, they behave differently for the long wave case $k \to 0$, see figures 10b) and 10d). It can be clearly seen that the interfacial modes tend slowly to an asymptotic neutral value of $\Im(\omega) = 0$, meanwhile the bulk ones reach the stability zone, $\Im(\omega) < 0$.

We also plot the convection rate $\Re(\omega)$ against the wavenumber for both modes, see figures 10e) and 10f). For short waves, notice that the curves adopt a straight line that follows the relation $\Re(\omega) \sim kU(\overline{y})$, which means that the perturbations are localised at a cross-channel position $\overline{y}$ and are convecting with the flow at velocity $U(\overline{y})$ (see [40]). For the interfacial modes (with $k > 2$), we obtain $\Re(\omega) \sim 0.9742\,k = U(0.8976)\,k$ for the case $\Gamma\Lambda = 0.003$, where $\overline{y} = 0.8976 \approx \kappa$ is extremely close to the value of the interface location. Similarly, for $\Gamma\Lambda = 0.005$, we obtain $\Re(\omega) \sim 0.9816\,k = U(0.867)\,k$, with $\overline{y} = 0.867 \approx \kappa$.

On the other hand, the perturbation of the bulk modes seem to be located very close to the interface location but on the yielded region ($y > \kappa$), as we

obtain the following relations that approximate well to our results: $\Re(\omega) \sim 0.9756\,k = U(0.8978)\,k$ for $\Gamma\Lambda = 0.003$, and $\Re(\omega) \sim 0.9770\,k = U(0.8693)\,k$ for $\Gamma\Lambda = 0.005$.

We also obtain the dispersion relations for a higher value of the shear-banding parameter $\theta = 0.60$, where the interfacial modes are dominant over the bulk ones, whose results are shown below in figure 11a). It can be clearly seen that now the interfacial modes (solid lines) are dominant for all values of the wavenumber.

The convection rate against wavenumber plot is shown in 11c), and we notice a behaviour similar to the one from figures 10e) and 10f): for very short waves, we can fit the results into a linear equation. For the interfacial modes (solid line), we get $\Re(\omega) \sim 0.9863\,k = U(0.889)\,k$, where the cross-channel position $\overline{y}$ is almost equal to the value of the interface location $\kappa = 0.8887$.

Finally, we show the dispersion relation of points that are part of the less unstable bulk mode B_2, which is present in the non-shear-banding zone (see figure 9). Results are shown in figure 12. Taking a fixed value of $\theta = 0.04$, we illustrate the dispersion relation for two cases: one with $\Gamma = 0.003$ (solid line) and another one with $\Gamma = 0.005$ (dashed line). The main conclusion we can obtain from these results is that the growth rate is negative in the long wave case $k \to 0$, meaning that we have a bulk mode. Above the critical shear-banding parameter value, this bulk mode becomes an interfacial mode, as we previously described in figures 9 and 10. From now on, when we talk about bulk modes, we will refer to those that are more unstable (B_1).

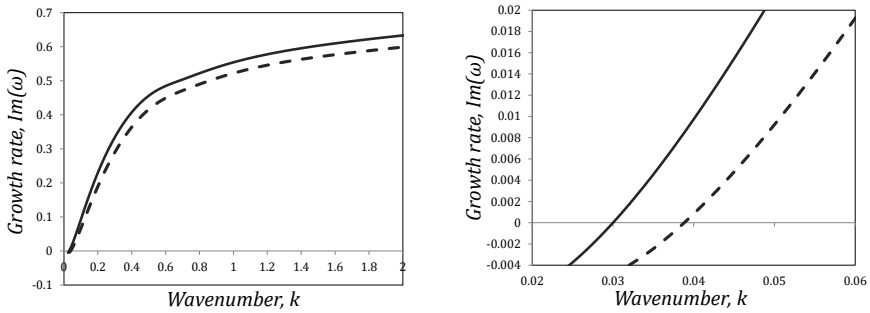

(a) $\Im(\omega)$ vs k

(b) $k \to 0$

Figure 12: Dispersion relations of the less unstable sinuous bulk mode (B_2 in figure 9). The parameter model values are $W = 2$, $\Lambda = 1$, $\theta = 0.04$ and $\Phi = 0.001$. The solid line has a value of $\Gamma = 0.003$ and the dashed line is for $\Gamma = 0.005$. Figure (b) shows the behaviour at very long waves.

4.1.3 Interfacial instabilities with continuity in the first normal stress difference predicted by the Oldroyd-B model

In the previous section, we discovered two unstable modes: bulk and interfacial instabilities. The first of these have been recently studied by [38] and by ourselves in previous works (without shear-banding), and the second modes have been also observed by multiple research groups [16, 39, 18, 11] in both Poiseuille and Couette shear-banded flows. The mechanism for these interfacial instabilities has been assumed to depend critically on a discontinuity in N_1 across the interface, as in the truly interfacial elastic instabilities first discovered in the 90's [22, 10]. In some cases, which include diffusion, N_1 is not strictly discontinuous, but there is always a rapid variation in N_1 across a small region [11, 18]. But for our fluid, N_1 is continuous and slowly varying across the shear-band interface.

The difference, as stated above, is that the instability for the interfacial modes observed by them seems to arise when elasticity varies discontinuously, which is not the case for the BMP model with shear-banding, see figure 5c). For these reasons, we decide to explore if the interfacial instabilities that we are observing in section 4.1.1 are also predicted by other models that are able to satisfy the conditions of continuity in N_1, and of course, a jump in viscosity at the interface.

We use a simple model that can help to achieve this, which is the Oldroyd-B model. In a previous work by Wilson & Rallison [41], this model was used to study the instability of elastic liquids where the concentration of the polymer C (which is proportional to its viscosity) changes across the channel of half-width L. We create an artificial scenario that emulates shear-banding phenomenon: a two-layer flow, where two fluids of different viscosities are separated by an interface located at some point $y = \kappa$ in the channel. The fluid near the centreline has a much higher viscosity than the fluid near the channel walls and although the two fluids have different Weissenberg number values, there is continuity of the first normal stress difference across the interface.

The full results can be found in appendix A. Here we briefly mention the main findings: an interfacial instability similar to the one predicted by the generalised BMP model (section 4.1.2) is also predicted by the Oldroyd-B model given the proper flow conditions, i.e. a jump in the fluid viscosity at the interface, along with continuity in the first normal stress difference. In addition, we found that the fluid elasticity is a key component of the instability: stability is seen at low values of Weissenberg number, while the opposite is observed if W is increased.

4.2 Sinuous and varicose modes

In the previous sections, we have been showing only sinuous perturbations. The reason for this is that in our previous work [9], we found that sinuous perturbations are slightly more unstable than varicose ones for long and intermediate waves, although both reach the same asymptotic value for short waves. Here we simply show that this still seems to hold when the shear-banding phenomenon is present, for both bulk and interfacial modes, see figure 13.

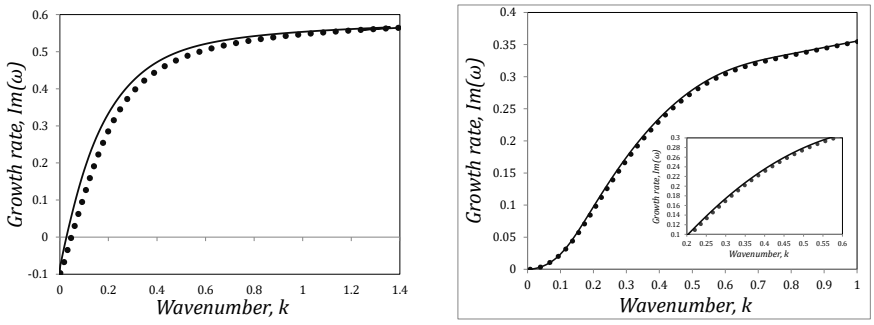

(a) Bulk modes (b) Interfacial modes

Figure 13: Growth rate $\Im(\omega)$ against wavenumber k for sinuous (solid lines) and varicose (dotted lines) perturbations, with $W = 2$, $\Phi = 0.001$, $\Lambda = 1$, $\Gamma = 0.003$ and $\theta = 0.118$ fixed. Figure (a): bulk modes. Figure (b): interfacial modes.

For the case of bulk modes, figure 13a), the dispersion relation for sinuous perturbations is slightly above the varicose ones, but stability is observed for both perturbations for long waves. For interfacial modes, figure 13b) is a bit more complicated to appreciate, as it seems that the sinuous curve is superimposed over the varicose one, but if we zoom in, we can see that indeed the sinuous perturbations tend to be more unstable.

4.3 Variable Weissenberg number

In our previous paper [9], we observed that the flow becomes unstable if the elastic relaxation time-scale λ_{ve} (and thus, the Weissenberg number) is large, and it becomes even more unstable if the order of magnitude of λ_{ve} is much higher compared to the structural relaxation time λ and the plastic time scale λ_{tp}. In this section, we show some examples of this behaviour, which still holds for both bulk modes with sinuous and varicose perturbations, as can be seen in figure 14.

As we concluded in the previous section, sinuous perturbations will be more unstable than varicose ones for either bulk and interfacial modes, and this becomes more evident when the Weissenberg number W is increased, as shown in

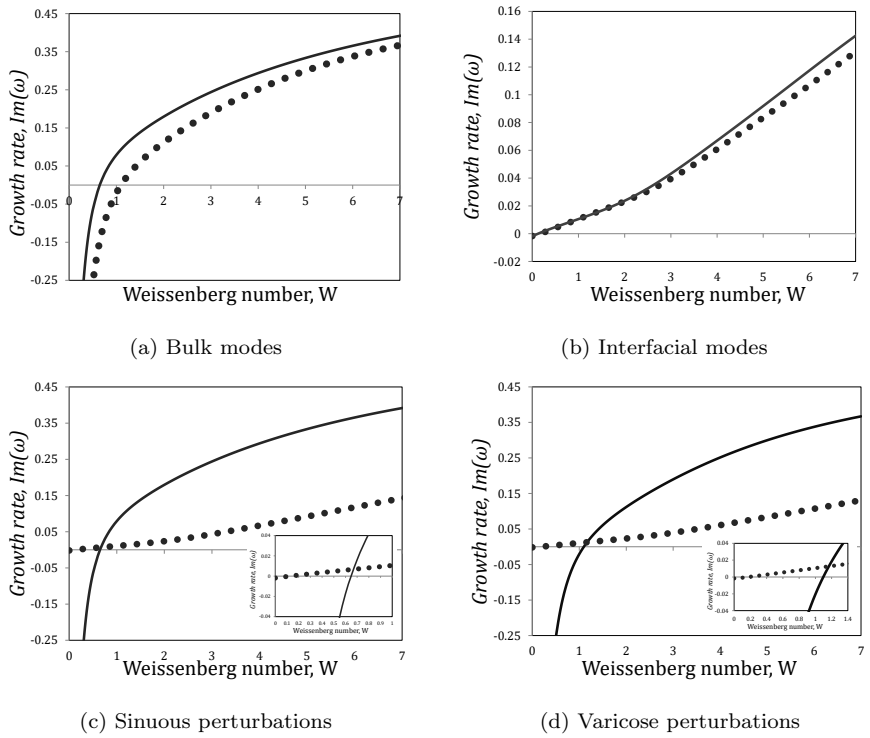

(a) Bulk modes

(b) Interfacial modes

(c) Sinuous perturbations

(d) Varicose perturbations

Figure 14: Growth rate $\Im(\omega)$ against Weissenberg number with $\theta = 0.1180$, $k = 0.1$, $\Gamma = 0.003$, $\Lambda = 1$ and $\Phi = 0.001$ fixed. Figure (a): bulk modes. Figure (b): interfacial modes. For figures (a) and (b): solid line is for sinuous perturbations and dotted ones for varicose perturbations. Figure (c): sinuous perturbations. Figure (d): varicose perturbations. For figures (c) and (d): solid lines are bulk modes and dotted lines are interfacial ones.

figures 14a) and 14b).

At low values of shear-banding parameter, $\theta = 0.118$, and with $k = 0.1$, $\Lambda = 1$, $\Gamma = 0.003$ and $\Phi = 0.001$ fixed, we compare the behaviour of the bulk and interfacial modes as the elastic relaxation time scale (proportional to W) grows, see figures 14c) and 14d). Notice that for sinuous perturbations with values of $W > 0.7$, the growth rate for the bulk modes is much higher compared to that for the interfacial instabilities. In addition, the thixoelastic number $W_{te} = W/\Lambda$ also becomes larger, meaning that the elastic effects overcome the thixotropic effects, leading to instability in both bulk and interfacial modes.

However, for values of $W < 0.7$, the bulk modes reach the stability zone, and the growth rate for interfacial modes is positive with an extremely small value $\Im(\omega) \approx 0.005$, which might indicate that for our very specific set of parameters chosen, the flow is initially slightly unstable due to an interfacial instability

at values of $W < 0.7$, but an increase in the Weissenberg number (and thus, of λ_{ve}) will completely lead to a bulk instability. In order to illustrate this, we calculate the *critical Weissenberg number* W_c defined as the dimensionless flow rate below which the flow is stable to perturbations of all wavenumbers (see [40, 8]). From our calculations, we got that the critical Weissenberg number for the sinuous interfacial mode is $W_c = 0.1105$ (with critical wavenumber $k_c = 1.312$), meanwhile, for the sinuous bulk modes, we obtain $W_c = 0.1562$ and $k_c = 0.837$, which indicates that indeed for our particular case of study ($\theta = 0.118$, $k = 0.1$, $\Lambda = 1$ and $\Phi = 0.001$), an interfacial instability will appear first. We get similar results for varicose perturbations: $W_c = 0.1217$ and $k_c = 1.75$ for interfacial modes, and $W_c = 0.252$ and $k_c = 1.74$ for bulk ones.

Although we have only reported just one case of study, we have found that these trends are robust to changes in the other dimensionless parameters.

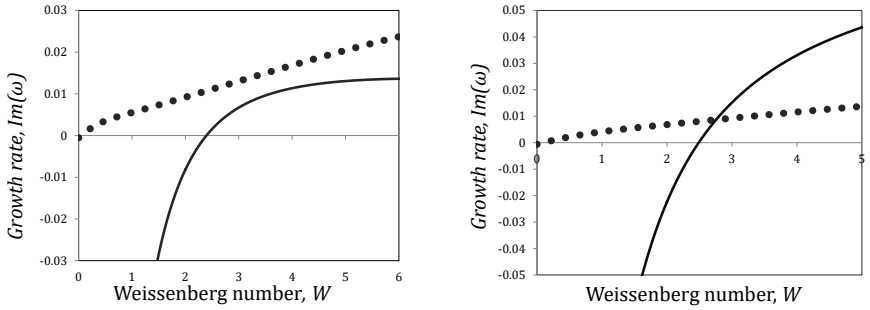

(a) Bulk modes

(b) Interfacial modes

Figure 15: Growth rate $\Im(\omega)$ against Weissenberg number for sinuous perturbations with $\theta = 0.60$, $\Phi = 0.001$, $k = 0.1$ and $\Lambda = 1$ fixed. The solid line represents the bulk modes, and the dotted one is for interfacial modes. Figure (a): $\Gamma = 0.003$ with $\kappa \approx 0.89$; figure (b): $\Gamma\Lambda = 0.02$ with $\kappa \approx 0.79$.

Moreover, it also seems that the interfacial modes might not only be caused by a jump in fluidity; elasticity is also a key factor here, as an increase in W involves a rise in the growth rate, for either varicose or sinuous perturbations. This is confirmed by the limit $W \to 0$ of the two-layer flows (see appendix A): elasticity is crucial to interfacial instabilities in the absence of inertia.

Lastly, we also compare the behaviour of the interfacial and bulk modes as the Weissenberg number increases but now with a higher value of shear-banding parameter value $\theta = 0.60$. Results can be seen in figure 15, where two comparative cases are reported: one in which the interface location is relatively close to the wall ($\Gamma\Lambda = 0.003$ with $\kappa \approx 0.89$) and another one in which the interface is slightly further away from the channel wall ($\Gamma\Lambda = 0.02$ with $\kappa \approx 0.79$). In contrast with the conclusions obtained from figure 14, for the former case, the interfacial modes will be more unstable than the bulk ones for any value of W. Additionally, we can observe that the growth rate for the interfacial mode

(dotted line) will be mostly positive (with the exception of the limit $W \approx 0$), meanwhile the bulk one is fully stable at $W < 1.5$.

On the other hand, if the interface is no longer so close to the wall, we can notice a similar behaviour to that of figure 14: the interfacial modes are weakly unstable but dominant over the bulk ones in the limit of very low Weissenberg number values, while bulk modes become much more unstable at $W > 2.8$. From these observations, we can deduce an important conclusion: the interface location determines whether a bulk or an interfacial mode is dominant.

4.4 Thixotropic timescales

We have studied flow instabilities and the effect of Φ, k, W and θ on them. In the following sections, we will discuss the effects of the parameters governing structural reformation (Λ) and destruction (Γ). We divide the subsections into two parts: 1) we first study the behaviour of the bulk modes, and 2) we focus on interfacial modes, making direct comparisons with respect to the conclusions obtained for the bulk modes.

4.4.1 Thixoviscous number: bulk modes

In figure 16 we plot the growth rate against the thixoviscous number Λ for different low values of shear-banding parameter θ, with $W = 2$, $\Gamma = 0.002$, $\Phi = 0.001$ and $k = 0.1$ fixed. The case $\theta = 0$ is depicted in figure 16a), which corresponds to a case that we studied in our previous paper, where we concluded that the flow is linearly stable at both extremes of thixoviscous number: the limit $\Lambda \to 0$, which is the equivalent of a Maxwell fluid with high viscosity ($\eta \approx 1/\Phi$). On the other hand at $\Lambda \to \infty$, the fluid has an extremely slow structural recovery, and thixotropy dominates over viscoelastic effects (low thixoelastic numbers, $\Lambda \gg W$). However, when this condition is not met, the flow can be extremely unstable, as seen in figure 16a).

Similar behaviour is observed for non-zero values of θ, as shown in figure 16b): the limits $\Lambda \to 0$ and $\Lambda \to \infty$ are stable, which confirms that thixotropy effects also stabilise flows when shear-banding is present. It is not surprising that an increase in shear-banding parameter value (from top to bottom) leads to less unstable flows until full stability for bulk modes is reached.

Notice that some of the most unstable flows are seen when shear-bands are present (dashed lines), whose interface location is slightly away from the wall ($\kappa \approx 0.8 - 0.9$), meanwhile flows with continuity in the fluidity profile tend to be more stable (see high Λ region). Additionally, the curves and their maximum are being displaced from left to right as θ increases. In order to explain this, we define a new dimensionless number, which is a ratio of two fluid time scales that compares the shear-banding effects over the thixotropic ones, which we will call

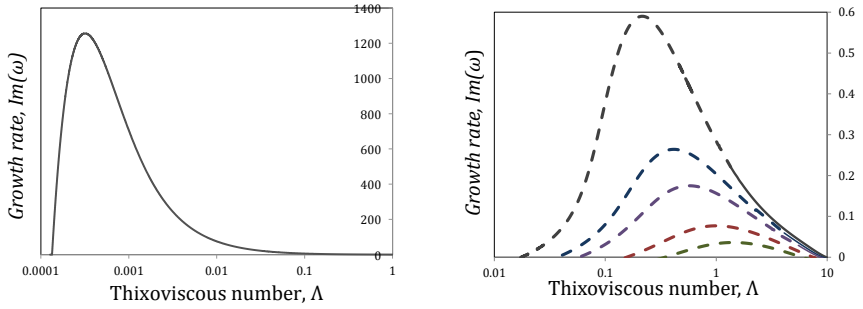

(a) $\theta = 0$ (b) $\theta \neq 0$

Figure 16: Growth rate plotted against the thixoviscous number Λ for $W = 2$, $\Gamma = 0.002$, $\Phi = 0.001$ and $k = 0.1$. Figure (a): case $\theta = 0$; (b): from top to bottom, $\theta = 0.07, 0.1, 0.1240, 0.20$ and 0.30. Dashed lines represent base-state shear-band flows.

ς:

$$\varsigma = \frac{\theta}{\Lambda} = \frac{\vartheta}{\lambda}. \tag{63}$$

We now reframe the growth rate from figure 16b) against ς, see figure 17. Notice that the instability is observed for intermediate values of ς, and the most unstable flows have roughly the same value of $\varsigma \approx 0.22$. It is important to point out that this interval is only valid for this case study ($\Gamma = 0.002$, $W = 2$, $k = 0.1$ and $\Phi = 0.001$), and will change if the other parameters take different values, but the conclusions obtained here will remain for bulk modes.

From this plot, we can get additional conclusions: for instance, in order to overcome the instabilities caused by elasticity, highly thixotropic fluids are required to stabilise the flow, as can be seen in the regions of low ς values (left side of the curve). On the other hand, we know that fluids with extremely quick structural reformation characteristics (low Λ) tend to be unstable, so in order to compensate for the lack of thixotropy, high shear-banding parameter values θ are needed to lead to stability of the bulk modes, or in other words, high ς values (right side of the curve). However, in the next subsection, we will see that this extreme involves unstable interfacial modes.

4.4.2 Thixoviscous number: interfacial modes

In this subsection, we focus on the regime where the interfacial instabilities are dominant over the bulk ones; this is seen when high values of shear-banding parameter are present. We simply carry out a similar analysis that was carried out in section 4.4.1 to study the dependence of the growth rate on the thixoviscous number for interfacial modes. Results can be seen in figure 18.

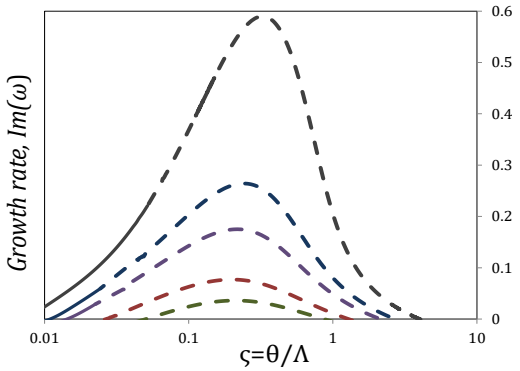

Figure 17: Growth rate $\Im(\omega)$ against ς for sinuous perturbations. The parameter values used are the same as in 16b).

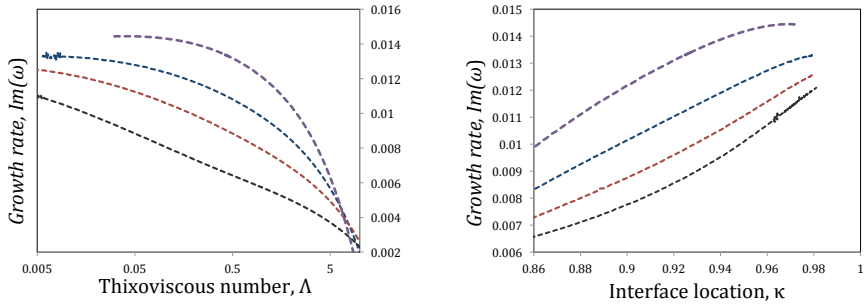

(a) $\Im(\omega)$ vs Λ

(b) $\Im(\omega)$ vs κ

Figure 18: Figure (a): growth rate plotted against thixoviscous number Λ for interfacial modes with $W = 2$, $\Gamma = 0.002$, $\Phi = 0.001$ and $k = 0.1$ fixed. Figure (b): growth rate against interface location κ. From top to bottom: $\theta = 0.30, 0.50, 1$ and 5.

In contrast with what we saw in figure 16, the behaviour of the modes is slightly different: although the modes get more stable as both θ and Λ increase, notice how a decrease in the thixoviscous number leads to highly unstable flows, which means that quick structural recovery is also dangerous for interfacial modes. Thus, interfacial modes are more dangerous at high values of the material time-scale ratio ς defined in equation (63). In addition, as we saw in figure 8, high shear-banding parameter values and small values of Λ lead to an interface location close to the channel wall, so we plot the growth rate against κ, see figure 18b), from which we can see that fluids whose interface location is very close to the wall $\kappa \approx 0.98$ are highly unstable. Unfortunately, we could not reach the limit $\Lambda \to 0$ as the no-slip condition at the channel wall is hard to satisfy as it involves extremely sharp velocity profiles in the base state. How-

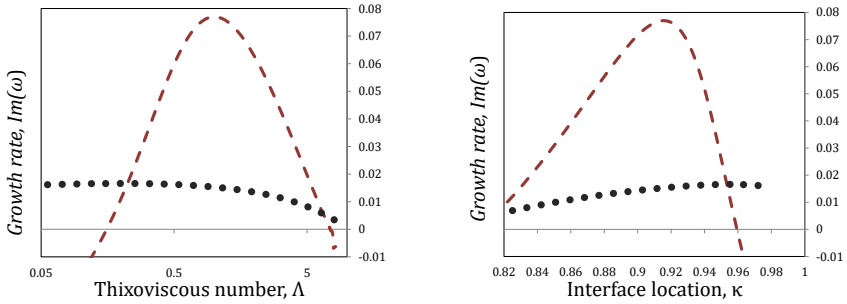

(a) $\Im(\omega)$ vs Λ (b) $\Im(\omega)$ vs κ

Figure 19: Behaviour of the interfacial (dotted line) and bulk (dashed lines) modes as a function of the thixoviscous number and the interface location. Figure (a): growth rate plotted against Λ for interfacial and bulk modes with $W = 2$, $\theta = 0.20$, $\Gamma = 0.002$, $\Phi = 0.001$ and $k = 0.1$ fixed. Figure (b): growth rate vs interface location κ.

ever, we can see that for the case $\theta = 0.30$ (curve at the top), the growth rate is slightly decreasing. We believe that the interfacial mode will become neutrally stable (or at least stable) when the interface location reaches the wall, $\kappa = 1$, as predicted by the Oldroyd-B model in appendix A.

Lastly, we simply compare the behaviour of the bulk and interfacial modes as a function of the thixoviscous number with fixed values $W = 2$, $\theta = 0.20$, $\Gamma = 0.002$, $\Phi = 0.001$ and $k = 0.1$, see figure 19. As concluded before, it can be clearly seen that although the interfacial modes are weakly unstable, they are dominant at very low values of thixoviscous number, which is the limit in which the interface location is very close to the wall (see figure 19b). The bulk modes, on the other hand, are dominant for intermediate values of thixoviscous number and can be highly unstable. Finally, both modes tend to be stable when the thixotropic effects dominate (large Λ).

4.4.3 Thixoplastic number: bulk modes

Now we focus on studying the effect of the destruction parameter on the bulk instabilities for different values of the shear-banding parameter. However, we will plot our results against the timescale associated with the destruction process: the thixoplastic number, previously defined as $W_{tp} = \sqrt{\Gamma\Lambda(1-2\Phi)}$. As explained before, each value of the thixoplastic number involves a unique base state, given that the base-state quantities depend on the product $\Gamma\Lambda$.

We fix the values of $k = 0.1$, $W = 2$, $\Phi = 0.001$, and we choose two representative cases of weakly thixotropic fluids: $\Lambda = 0.1$ and $\Lambda = 0.2$. Results are shown in figure 20.

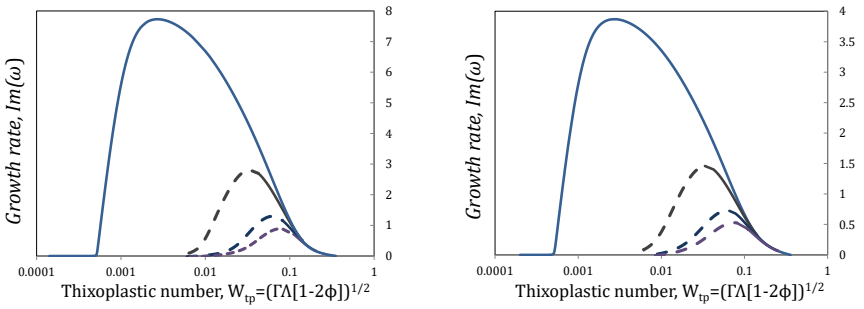

(a) Case $\Lambda = 0.1$ (b) Case $\Lambda = 0.2$

Figure 20: Growth rate plotted against thixoplastic number W_{tp} for bulk modes with $W = 2$, $\Phi = 0.001$ and $k = 0.1$ fixed. Figure (a): $\Lambda = 0.1$; (b): $\Lambda = 0.2$. From top to bottom: $\theta = 0, 0.05, 0.1$ and 0.1240. Solid lines represent base-states with continuity in the fluidity profiles, meanwhile dashed lines indicate a jump in the shear rate at the interface location.

The curves that are found at the top in figures 20a) and 20b) are the cases with $\theta = 0$ that have been previously studied [9]. Similarly to figure 16a), the extremes $W_{tp} \to 0$ and $W_{tp} \to \infty$ are both stable; the first limit is the equivalent of a Maxwell fluid with low fluidity $\varphi = \Phi$, and the second limit involves high structural destruction and a growth of the yielded region near the walls. Additionally, as reported in [9], the most unstable base state for fixed Φ, Λ, W, k and $\theta = 0$ is found when the dimensionless critical stress $\tau_c = 1/W_{tp}$ is located near the channel wall (around $y \approx 0.98$).

For non-zero values of the shear-banding parameter, the curve behaviour does not change: it is not surprising that an increase in θ stabilises the flows, and the limits $W_{tp} \to 0$ and $W_{tp} \to \infty$ are stable as well. In addition, the most unstable base states for fixed $\theta \neq 0$ satisfy the condition that the critical stress σ_c (whose value is slightly greater than the stress plateau σ_p) is still close to the wall. The difference with respect to the case $\theta = 0$ is that a rise in θ diminishes the shear rate and shear stress at $y = 1$, and thus, the critical stress is displaced away from the channel wall. For instance, the most unstable state with fixed $\Lambda = 0.2$ for $\theta = 0.05$ has a value of $\tau_c = 29.91$ and is located at $y = 0.942$; for $\theta = 0.10$, $\tau_c = 16.15$ at $y = 0.904$, and for $\theta = 0.1240$, $\tau_c = 13.32$ located at $y = 0.888$. We also notice that for the cases where $\theta \neq 0$, the most unstable base states are seen when the transition from continuity (solid lines) to a jump in the fluidity profiles (dashed lines) occurs, or in other words, the slope of the curve φ vs y is extremely high (see section 3.2).

It is also evident that Λ plays a key role in the bulk instability, as it can be seen that all the curves from figure 20a) are much more unstable than the ones in 20b). This behaviour will be explored later.

Lastly, we made a similar analysis to the one made in figure 17: we define a new dimensionless quantity, ϖ, which is a material parameter simply defined as the ratio of two timescales; the time scale representative of plasticity and that for shear-banding effects:

$$\varpi = \frac{W_{tp}}{\theta} = \frac{\lambda_{tp}}{\vartheta}. \tag{64}$$

We now simply plot the growth rate of figure 20 against ϖ. The results are shown in figure 21.

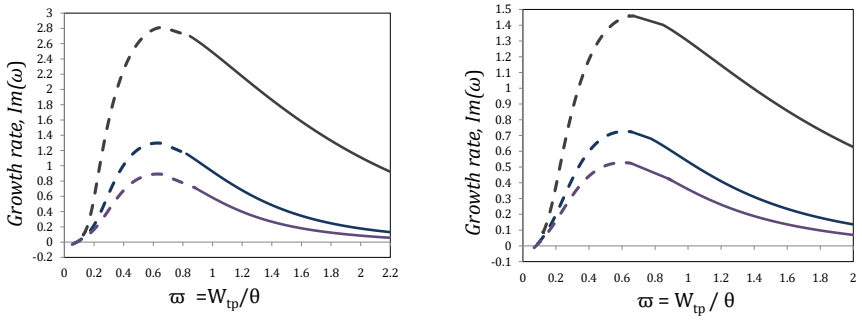

(a) Case $\Lambda = 0.1$ (b) Case $\Lambda = 0.2$

Figure 21: Growth rate plotted against ϖ for bulk modes. The model parameter values used are the same that the ones used in figure 20.

We can deduce that high thixoplastic numbers (i.e. when the yielded region grows along the channel) would lead to flow stability, so in order to compensate for weak shear-banding effects, which are usually unstable, high ϖ values are required to stabilise the flow (right side of the plots).

For the other extreme of low thixoplastic numbers, a similar conclusion is obtained: in order to overcome elastic effects and plasticity, low ϖ values are needed to stabilise bulk modes (we will see in the next subsection that this condition will lead to more unstable interfacial instabilities though). More interestingly, intermediate values tend to be highly unstable and the most unstable base-states for all the curves have the same value of ϖ: for both cases, $\Lambda = 0.1$ and $\Lambda = 0.2$, the most unstable flows are observed when $\varpi \approx 0.66$. The limit of this instability is the case $\theta = 0$, which we know beforehand is the most unstable case.

4.4.4 Thixoplastic number: interfacial modes

Now we focus on studying the effect of variable destruction parameter at high values of the shear-banding parameter, which is the regime in which the interfacial modes are more dominant over the bulk ones. We carry out a similar analysis to that in section 4.4.2: we fix the Weissenberg and thixoviscous number, the thixotropic ratio and the wavenumber, and we choose a set of three

values of shear-banding parameter $\theta = [0.5, 1, 5]$, and for each case, we vary Γ. We then plot the growth rate against the timescale characteristic of the destruction process, the thixoplastic number and against the interface location, see figure 22.

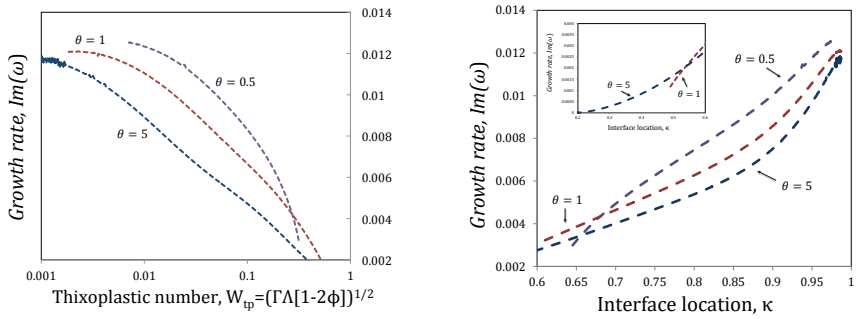

(a) $\Im(\omega)$ vs W_{tp}

(b) $\Im(\omega)$ vs κ

Figure 22: Figure (a): growth rate plotted against thixoplastic number W_{tp}; (b): growth rate against interface location. The parameter values $W = 2$, $k = 0.1$, $\Phi = 0.001$ and $\Lambda = 1$ are fixed. From top to bottom: $\theta = 0.5, 1$ and 5.

Similarly to the conclusions obtained from figure 18, the most unstable base-state flows seem to be the ones whose interface location κ is near the wall, and this is achieved when very low values of thixoplastic number (and therefore, low values of the material time scale ratio ϖ defined in equation (64)) are present. However, it was not possible to get to the limit $\kappa \to 1$ due to the sharp velocity profiles. This is evident for the case $\theta = 5$ (bottom curve of figure 22a), where there are some fluctuations due to numerical errors.

As expected, the curves with higher θ value are the less unstable ones. Moreover, we can see that for the curve with the lowest value of shear-banding parameter $\theta = 0.5$ (top curve), the interfacial mode only exists if the interface location is between $0.64 < \kappa < 1$, and it becomes stable at $W_{tp} \leq 0.32$, which coincides with the transition (in the base state) to a continuous fluidity profile. For the other cases, the interfacial modes will still be present for high thixoplastic numbers; for $\theta = 1$, the mode is seen at $W_{tp} \leq 0.6324$ with interface location $0.45 < \kappa < 1$ and lastly, for $\theta = 5$, instability is observed for $W_{tp} \leq 2.41$ with interface location $0.1841 < \kappa < 1$ (see small plot in figure 22b)).

Finally, as we did in section 4.4.2, we compare the behaviour of the bulk and interfacial modes as a function of the thixoplastic number with fixed values of $\theta = 0.10$, $k = 0.1$, $W = 2$, $\Lambda = 1$ and $\Phi = 0.001$. Results are shown in figure 23, where we can see that in the limit $W_{tp} \to 0$, the bulk modes (dashed lines) are fully stable, while the interfacial modes are weakly unstable.

From the results obtained here and in section 4.4.2, we can conclude that the interfacial modes become more unstable and dominant over the bulk modes if

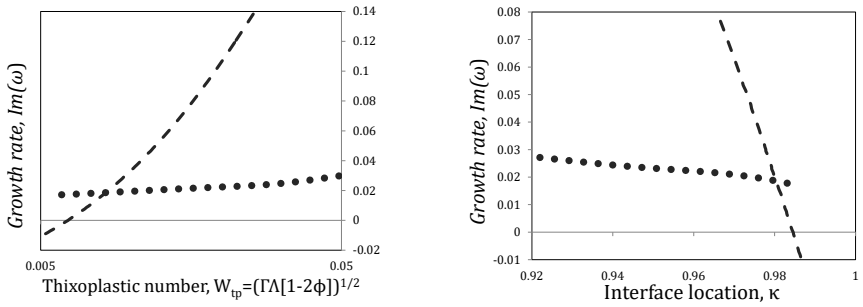

(a) $\Im(\omega)$ vs W_{tp}

(b) $\Im(\omega)$ vs κ

Figure 23: Behaviour of the interfacial (dotted line) and bulk (dashed lines) modes as a function of the thixoplastic number and the interface location. Figure (a): growth rate plotted against W_{tp} for interfacial and bulk modes with $W = 2$, $\theta = 0.10$, $\Lambda = 1$, $\Phi = 0.001$ and $k = 0.1$ fixed. Figure (b): growth rate vs interface location κ.

the interface location κ is very close to the wall, and small values of destruction parameter and thixoviscous number lead to instability, which is the equivalent of small values of the product $\Gamma\Lambda$: either small destruction and/or poor thixotropy are dangerous, which also satisfies the condition obtained in equation (62).

4.4.5 Thixoplastic number at fixed shear-banding parameter: bulk modes

In this final subsection, we now explore the behaviour of variable thixoplastic number with a fixed shear-banding parameter in bulk modes with sinuous perturbations. In our previous publication [9], we analysed this case and we will briefly explain here what we found. We know that intermediate values of thixoplasticity tend to be unstable, and they become more dangerous if the viscoelastic time scale is much larger than the structural relaxation time scale, $\lambda_{ve} \gg \lambda$. Thus, λ plays a key role in the bulk instability. For that reason, we studied the effect of the thixoplastic number on the growth rate with multiple combinations of the destruction and reformation parameters. In order to make things easier for the reader, the results obtained in [9] are shown in figure 24.

We took a set of fixed values for $\Lambda = \{0.1, 0.2, 0.5, 1\}$, and for each case, we calculated the growth rate as a function of the thixoplastic number, by varying the destruction parameter Γ, see figure 24a).

The main conclusions we obtained are that there is a strong dependence of the growth rate of the instability on the reformation parameter Λ, as the instability becomes more dangerous when Λ decreases (bottom to top). Additionally, the most unstable point of each curve has the same value of thixoplastic

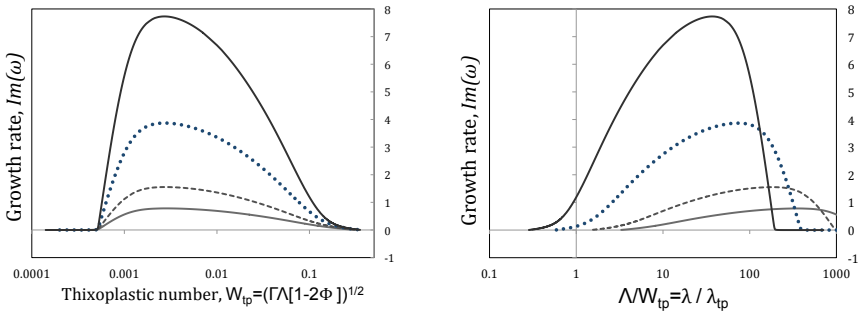

(a) Varying thixoplastic number

(b) Varying Λ/W_{tp}

Figure 24: Dependence of growth rate of bulk sinuous perturbations on thixoplastic number, at fixed $W = 2$, $\Phi = 0.001$, $k = 0.1$ and $\theta = 0$. For each curve Λ is constant and Γ varies. Main plots, top to bottom: $\Lambda = 0.1$, 0.2, 0.5 and 1. (a) Growth rate against thixoplastic number; (b): growth rate against the ratio Λ/W_{tp}. These results were originally reported in [9].

number, which is around $W_{tp} = 0.00269$, which indicates that there is a small yielded region near the wall ($0.98 < y < 1$), and the critical stress τ_c is located at $y \approx 0.98$.

We can also appreciate the strong dependence of the instability on Λ and Γ in figure 24b), where we plot the growth rate against the material parameter Λ/W_{tp}, which is the ratio of the thixotropic and plastic timescales. From this plot we deduced that the instability follows the scaling $\Im(\omega) \propto \Lambda^{-1} \propto \Gamma$, and the most unstable points of each curve can be fitted to a single power-law equation that adopts the following form:

$$\Im(\omega) = A\,(\lambda/\lambda_{tp})^{-n}, \tag{65}$$

where A and n are coefficients that depend on the Weissenberg number, wavenumber, thixotropic ratio and, as we will see soon, on the shear-banding parameter.

The characteristics of the instability described above are still seen for bulk modes with non-zero shear-banding parameter values, as illustrated in figure 25, where we show two different cases: $\theta = 0.1$ and $\theta = 0.1240$. Firstly, we focus on figures 25a) and 25b), where the growth rate is plotted against thixoplastic number. It can be seen that the behaviour of these curves resembles the one observed in the zero shear-banding case 24a): there is a most dangerous thixoplastic number, and therefore, a most dangerous base-state flow for each value of θ; for $\theta = 0.1$, $W_{tp} \approx 0.062$, whose interface is located at $\kappa \approx 0.8791$ with stress plateau value $\sigma_p \approx 15.71$ and critical stress value $\tau_c \approx 16.15$ located at $y = 0.903$, meanwhile for $\theta = 0.1240$, $W_{tp} \approx 0.075$ with interface location $\kappa = 0.8618$, $\sigma_p = 12.94$ and critical stress $\tau_c = 13.31$ located at $y = 0.8871$. Furthermore, we obtain the dispersion relation for these highly unstable flows, and from the plot $\Re(\omega)$ vs k, we were able to obtain the location of the perturbation

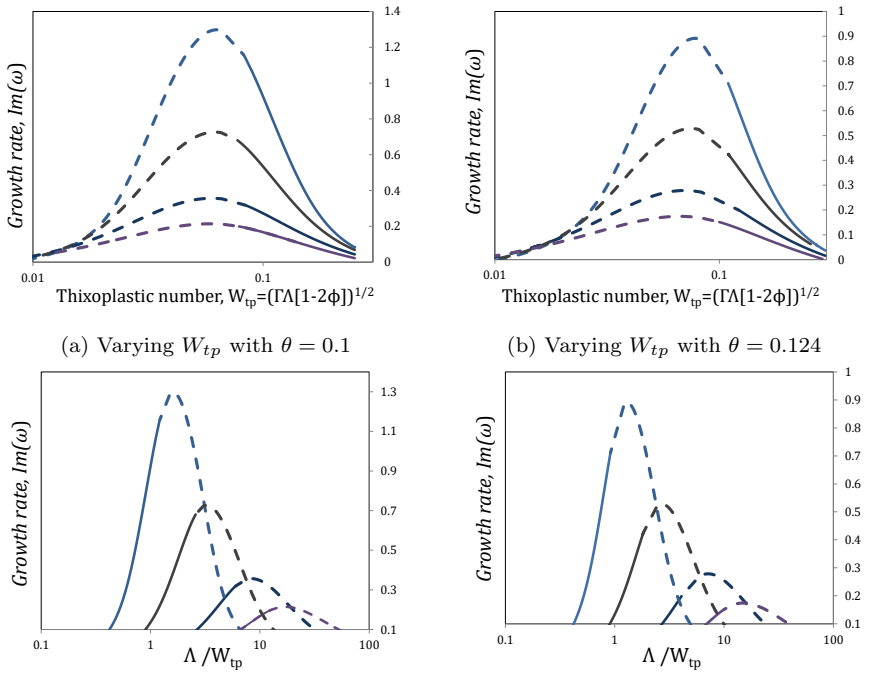

(a) Varying W_{tp} with $\theta = 0.1$

(b) Varying W_{tp} with $\theta = 0.124$

(c) Varying Λ/W_{tp} with $\theta = 0.1$

(d) Varying Λ/W_{tp} with $\theta = 0.124$

Figure 25: Figures (a) and (b): growth rate against thixoplastic number for bulk modes with shear-banding parameter variable fixed. Figures (c) and (d): growth rate plotted against material parameter Λ/W_{tp} with fixed θ. For all plots: $W = 2$, $k = 0.1$ and $\Phi = 0.001$; from top to bottom: $\Lambda = 0.1, 0.2, 0.5$ and 1. Dashed lines represent base-states with a jump in the fluidity profile.

(as we did in section 4.1.2). The results show what we have concluded before: bulk perturbations are located in the yielded region which is near the channel wall; more specifically, we found that the perturbation is located roughly in the same position in which the critical stress value is. For the case with $\theta = 0.1$, the perturbation is found at $y = 0.892613$, while for $\theta = 0.1240$, it is located at $y = 0.8871$.

We also note the strong dependence of the instability on the thixoviscous number, and in order to appreciate this better, we reframe these results instead in terms of the material parameter Λ/W_{tp}, see figures 25c) and 25d). Similarly to the case $\theta = 0$, figure 24b), the maximum growth rate shifts to the left as Λ decreases, which is consistent with what we have concluded in our previous work: fluids that exhibit quick structural reformation are highly unstable. For very large values of Λ/W_{tp} the flow tends to be stable; this is a limit where thixotropy dominates. The instability for non-zero shear-banding parameter values for bulk modes follows the scaling previously found: $\Im(\omega) \propto \Lambda^{-1} \propto \Gamma$, which establish

that highly unstable flows are observed when the following condition is satisfied: high thixoelastic and elastoplastic numbers or $\lambda_{ve} \gg \lambda_p \gg \lambda$. In addition, as concluded in section 4.4.3, intermediate values of the material time-scale ratio $\varpi = W_{tp}/\theta$ are present for the most unstable flows with bulk modes, which means that these time-scales are of the same order of magnitude: $\lambda_{tp} \approx \vartheta$.

As explained before, the maximum values of growth rate and their respective values of Λ/W_{tp} from figures 25c) and 25d) can be fitted to a single power-law equation. For the case $\theta = 0.1$, $\Im(\omega) = 1.8045(\lambda/\lambda_{tp})^{-0.756}$ with $R^2 = 0.99912$, meanwhile $\Im(\omega) = 1.0285(\lambda/\lambda_{tp})^{-0.659}$ with $R^2 = 0.99937$ for $\theta = 0.1240$. If we compare these coefficients with the zero-shear banding parameter case, where $\Im(\omega) = 370.92(\lambda/\lambda_{tp})^{-1}$, it can clearly be seen that the power-law coefficient of these functions is decreasing as θ increases, and is also a function of Λ, Γ, Φ, k and W.

We also have determined that for fixed values of our model parameters, the index n cannot be larger than 1. We demonstrate this empirically by looking at the same parameter values used for the zero-shear banding parameter case. We calculated the maximum values of growth rate for the most dangerous base state for a higher value of wavenumber, $k = 0.7$, which corresponds to a highly dangerous wavenumber when $\theta = 0$, and we obtained the following power-law equation: $\Im(\omega) = 309.17(\lambda/\lambda_{tp})^{-0.999}$ with $R^2 = 1$.

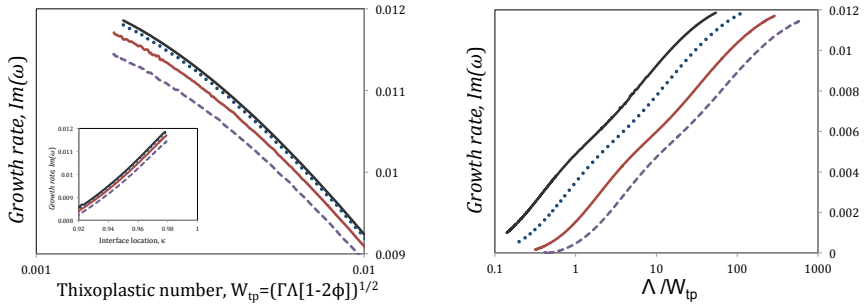

(a) Varying thixoplastic number

(b) Varying Λ/W_{tp}

Figure 26: Figure (a): dependence of growth rate of interfacial sinuous perturbations on thixoplastic number. The inset shows the growth rate versus interface location. Figure (b): growth rate plotted against the material time-scale ratio Λ/W_{tp}. For both figures, we fix $W = 2$, $\Phi = 0.001$, $k = 0.1$ and $\theta = 5$. For each curve Λ is constant and Γ varies. Top to bottom: $\Lambda = 0.1$, 0.2, 0.5 and 1.

Lastly, we explore the behaviour of variable thixoplastic number at fixed shear-banding parameter in the interfacial modes. As we did with the bulk modes, a set of fixed values for $\Lambda = \{0.1, 0.2, 0.5, 1\}$ is taken and for each case, we calculate the growth rate as a function of the thixoplastic number, by varying the destruction parameter Γ. Results are shown in figure 26a). It is not surprising to see that the most unstable flows are located near the channel wall,

and this is observed in the limit of small thixoplastic number ($W_{tp} \propto \Gamma\Lambda \to 0$). Moreover, we notice that although a decrease in the thixoviscous number (from bottom to top) is destabilising, the growth rate values do not rocket like in the bulk modes. In fact, the interfacial modes do not follow the scaling observed for the bulk perturbations, see equation (65): they follow the opposite behaviour, see figure 26b). In contrast to what we observed in figure 25 for the bulk modes, the interfacial modes become slightly more unstable when the material time-scale ratio Λ/W_{tp} is large, or in other words, the structural relaxation time is much larger than the plastic time scale, $\lambda \gg \lambda_{tp}$. In addition, as concluded in section 4.4.4, these interfacial modes will dominate at low values of the material time scale ratio ϖ, or in other words, if the following condition is satisfied: $\lambda_{tp} \ll \vartheta$.

4.5 Streamlines of the most unstable flows

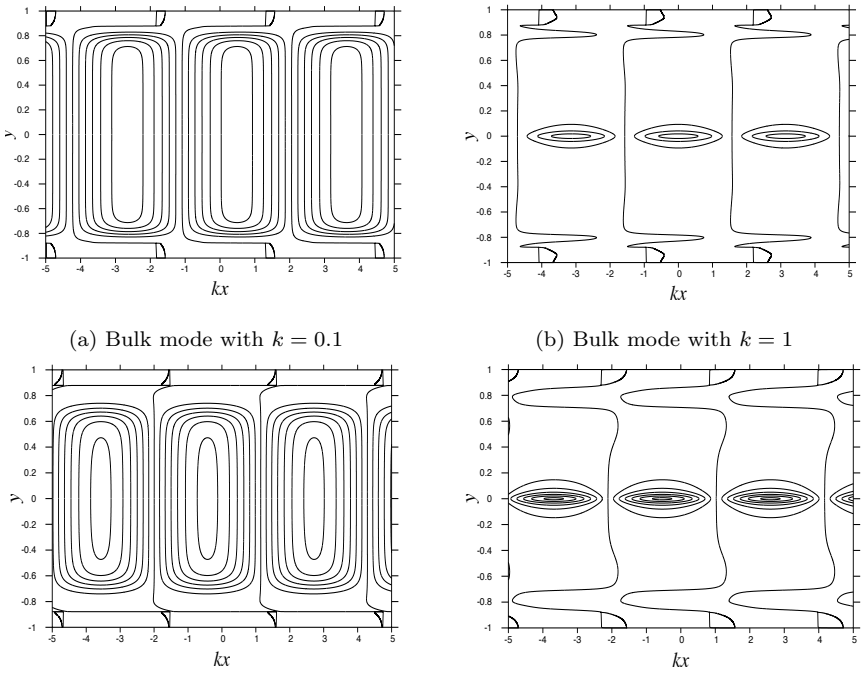

(a) Bulk mode with $k = 0.1$

(b) Bulk mode with $k = 1$

(c) Interfacial mode with $k = 0.1$

(d) Interfacial mode with $k = 1$

Figure 27: Streamlines of the perturbation flows for the unstable sinuous bulk and sinuous interfacial modes for different values of wavenumber k. The parameter values used are $W = 2$, $\Phi = 0.001$, $\Lambda = 0.20$, $\theta = 0.1$ and $\Gamma = 0.0192$. The interface location is $\kappa = 0.8791$.

In this final subsection, we show the streamlines of the perturbation flows

for unstable bulk and interfacial modes, see figure 27. For the former case, we choose the most unstable flow for the case of $\theta = 0.10$ and $\Lambda = 0.20$ (shown in figure 25a). The other parameter values for this case are $\Gamma = 0.0192$, $W = 2$, $\Phi = 0.001$ and $k = 0.10$. For this set of parameter values, the bulk mode is dominant over the interfacial mode, and we can find the streamlines of this unstable bulk mode in figure 27a), where we can see that within the unyielded region near the centreline, there is only vertical motion, which means that the component of the perturbed velocity in x-direction is zero. However, near the interface location ($\kappa = \pm 0.8791$), we observe fluid motion in both x-and y-direction. More interestingly, we can see reverse flow near the channel wall. If we increase the wavenumber to $k = 1$ (which leads to more unstable flows), this becomes more evident, as illustrated in figure 27b). The general behaviour away from the wall also changes: there are sections in the channel in which only vertical motion is observed, but motion in both directions is seen close to the centreline.

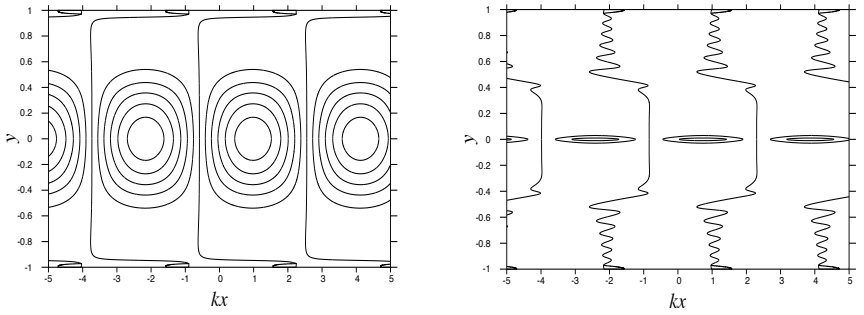

(a) $k = 0.1$ (b) $k = 1$

Figure 28: Streamlines of the perturbation flows for the unstable sinuous interfacial modes for different values of wavenumber k. The parameter values used are $W = 2$, $\Phi = 0.001$, $\Lambda = 0.20$, $\theta = 0.5$ and $\Gamma = 0.00032$. The interface location is $\kappa = 0.9714$.

We also show the streamlines of the interfacial modes with the same parameter model values used to obtain figures 27a) and 27b). Although the bulk modes are more unstable than the interfacial perturbations, the latter ones are unstable as well. For the case $k = 0.1$ (see figure 27c), vertical motion is seen in the unyielded region near the centreline (similarly to what we observed in figure 27a). As we approach the interface location, we notice that there are non-zero values of the perturbed vector velocity in both directions (u and v). The major difference with respect to the bulk modes is that we can observe purely horizontal motion exactly at $\kappa = 0.8791$. In the yielded region, reverse flow is also observed.

If we increase the wavenumber to $k = 1$ (figure 27d), we obtain a similar picture to that of the bulk mode (figure 27b). However, notice that the direction

of the perturbed flow near the interface location is different.

We now choose parameter values for which the interfacial modes are dominant over the bulk ones. In order to meet this condition, we previously concluded that low values of $\Gamma\Lambda$ and high values of θ are needed. In this way, we choose $\Gamma = 0.000032$, $\Lambda = 0.20$ and $\theta = 0.50$, which gives an interface location value of $\kappa = 0.9714$. The other parameter values are $W = 2$, $\Phi = 0.001$. The streamlines for $k = 0.1$ are shown in figure 28a). Unlike the case for the bulk mode shown in figure 27a), we can observe motion in both directions near the centreline. As we move away from this zone and before reaching the interface location, the x-component of the perturbed velocity field is almost null. In the narrow yielded region $1 > y > \kappa = 0.9714$, we can also observe reverse flow. If the wavenumber is increased to $k = 1$ (figure 28b), the phenomenon is still present and the flow becomes even more unstable, as fluctuations in the streamlines are observed in the unyielded region close to the interface location.

5 Conclusions

We extended our previous theoretical work carried out in [9] by studying the stability in pressure-driven channel flow of materials that exhibit shear-banding along with viscoelasto-thixo-plasticity. We used the generalised BMP model, which is an extension of the original model [2] and has been extensively used to describe complex rheological behaviour.

We obtained a set of dimensionless groups (Φ, Λ, Γ) from which we constructed key dimensionless quantities that were extremely useful in our previous work to describe the phenomena of viscoelasticity, thixotropy and plasticity present in our material. Alongside those dimensionless quantities, we have derived a new dimensionless number that can be incorporated to the family of timescales proposed by Ewoldt & McKinley [14]: the dimensionless shear-banding parameter, θ, from which we derived more dimensionless quantities for analysis of our results.

We have obtained semi-analytical solutions for the base state quantities for the cases with non-zero shear-banding parameter values that allow us to calculate velocity and fluidity profiles, along with the stress plateau and the interface location. We also provide a physical analysis of the large variety of base states that can be predicted by the combination of our fluid parameters.

We have made an extensive exploration of our model parameters and we have identified key conditions for flow instability/stability. Some of the conditions reported in [9] still hold for fluids that exhibit shear-banding, such as a decrease in the thixotropic ratio and an increase in the wavenumber leading to instabilities, and the limits $k \to 0$ and $W \to 0$ are stable. We have found that for fixed values of thixotropic ratio, wavenumber, Weissenberg number and destruction and reformation parameters, the fluids with $\theta = 0$ are always more

unstable compared to those with $\theta \neq 0$, i.e. an increase In θ will lead to less unstable flows, as there is a decrease of the shear rate and shear stress values at the channel walls. We have also identified two modes of instability: one of them, a highly unstable *bulk* mode B_1, which exists at $\theta = 0$ and is still present in the two flow regimes: a) where there exists continuity in the fluidity profile, and b) where we have a jump in the shear-rate, i.e. the presence of two bands of fluid that coexist with different shear-rate values at a given stress value. A second mode, which we call the *interfacial* mode was also found, whose perturbation is located at the plateau interface. This mode behaves as an interfacial mode in the flow regime b), but it becomes a bulk mode B_2 in the regime a), which happens to be less unstable than the previously described mode B_1.

Although is not possible to define a general criterion in terms of all our parameters that allow us to determine the onset of instability, we have identified key flow conditions in which one of the modes dominate over the other one: for fixed values of thixotropic ratio, Weissenberg number destruction and reformation parameters, we have observed that the bulk modes are dominant over the interfacial ones at very low values of shear-banding parameter and we concluded that the shear-thinning behaviour is an essential component of the bulk instabilities. On the other hand, interfacial modes will dominate for very large θ values, and they will start to replace the bulk modes when the shear-thinning characteristics of the low-shear-rate band vanish. This is expected to happen when the following condition is present: $\dot{\gamma}_1^2(1 + \theta\dot{\gamma}_1) \ll \Phi/\Gamma\Lambda$, where $\dot{\gamma}_1$ is the dimensionless shear rate value of the high viscosity band that coexists with the low viscosity band when the system reaches the stress plateau σ_p.

We have also identified additional dissimilarities and similarities between bulk and interfacial modes: for the latter case, the growth rate becomes neutrally stable at very long waves limit, $k \to 0$, meanwhile the bulk modes are fully stable in the same limit. The sinuous perturbations are always going to be slightly more unstable than the varicose ones for both modes, and for short waves, the perturbations will be localised very close to the location of the interface κ for interfacial modes, meanwhile, the perturbations for the bulk modes will be localised in the yielded region $y > \kappa$. More importantly, we determined that the viscoelastic effects are the main cause of instability for both bulk and interfacial modes, as an increase in W leads to unstable flows; for the former case, the instability vanishes when the limit $W \to 0$ has been reached, while for the latter case, the growth rate becomes neutrally unstable at $W = 0$.

We have also shown that the interfacial instability predicted by the generalised BMP model, which does not exhibit a jump in the normal stress difference at the interface, is also predicted by a much simpler rheological model: the Oldroyd-B model.

We explored multiple combinations of the thixotropic timescales derived from the generalised BMP model. For bulk modes, we found that fluids with very low values of thixoviscous number (extremely quick structural relaxation time) tend to be highly unstable, which is something we initially observed for

the case $\theta = 0$. We also found that instability will be observed for intermediate values of two new material parameters: a) ς, defined as the ratio of the dimensionless timescales θ and Λ (equivalent to the ratio ϑ/λ), which compares shear-banding and thixotropic effects and b) ϖ, defined as $\varpi = W_{tp}/\theta = \lambda_{tp}/\vartheta$ (ratio of plastic and shear-banding effects). The extremes of these material parameters $\varsigma \to 0$, $\varsigma \to \infty$ and $\varpi \to 0$, $\varpi \to \infty$ are stable.

For the interfacial modes, on the other hand, which tend to be dominant at high values of the shear-banding parameter and when the interfacial location is very close to the channel wall, we have observed unstable flows if the location of the interface κ is extremely close to the wall. This happens when $\Gamma\Lambda \to 0$, which means that either poor thixotropy (low Λ) and/or poor structural destruction (low Γ) is dangerous.

Lastly, for bulk modes, we found that there is a most dangerous thixoplastic number for each value of shear-banding parameter θ. The most dangerous W_{tp} depends on the values of k, W and Φ, but overall, we have found that intermediate values of thixoplastic number (where the yielded region near the wall grows) lead to the most unstable flows. Under these conditions, this bulk instability becomes even more dangerous if the thixoviscous number is allowed to decrease and if the viscoelastic relaxation time λ_{ve} is much longer than both the structural destruction timescale λ_{tp} and the thixotropic timescale λ:

$$\lambda \ll \lambda_{tp} \ll \lambda_{ve}. \tag{66}$$

In other words, instability is enhanced by extremely high elastoplastic and thixoelastic numbers. This condition for the time scales was originally found in our previous paper [9], and although an increase in θ leads to less unstable flows, we have shown here that this condition for instability still holds for non-zero shear-banding parameter values. In addition, we have observed that the most unstable flows satisfy the condition of intermediate values of the material time-scale ratio $\varpi = W_{tp}/\theta$, or in other words, ϑ and λ_{tp} are of the same order of magnitude:

$$\vartheta \approx \lambda_{tp}. \tag{67}$$

On the other hand, we have found that the interfacial modes follow a different time-scale condition: given an unstable flow for a given value of k, W and Φ, the interfacial instabilities become more dangerous if the structural relaxation time-scale is much bigger than that of plasticity, $\lambda \gg \lambda_{tp}$ and at very low values of ϖ and large values of ς, which leads us to propose the following condition of time-scale parameters for unstable interfacial modes with non-zero values of Weissenberg number:

$$\vartheta \gg \lambda \gg \lambda_{tp}. \tag{68}$$

We have provided evidence that interfacial modes dominate at low values of W, Γ and Λ, which leads us to think that for fluids that exhibit the shear-banding phenomenon ($\vartheta \neq 0$), a gradual startup flow of these fluids will be initially unstable due to an interfacial instability, but this can be followed by a bulk

instability if the time-scale conditions (66)–(67) are met. On the other hand, interfacial instabilities will only be observed if the model parameters satisfy equation (68).

It is worth mentioning that our results were obtained by using a constitutive equation that predicts a smoothly-varying continuous function for the first normal stress difference, in contrast with other works where the instability was driven by a jump in N_1 [36, 38, 16, 39]. Additionally, Cromer *et al.* [11] and Fielding *et al.* [18] also studied channel flows of shear-banding micellar solutions and both included diffusive effects in their respective constitutive equations and showed that diffusion has a stabilising effect. Although they predicted an instability without any true jumps in N_1, the mechanism of the instability observed by them is interfacial in nature; even with diffusion there will be relatively steep local gradients in N_1, while for the BMP model, we always have that $\mathrm{d}N_1/\mathrm{d}y = 4W\mathcal{P}^2 y$ (see equation (34)), which is a truly smooth function.

Lastly, we wish to mention that this paper leaves some questions open to future work. For instance, it is still necessary to study the behaviour of bulk and interfacial modes in the short-wave limit ($k \to \infty$) and at extremely high values of Weissenberg number to determine whether our conclusions obtained here still hold. It would also be of great interest to use a model that can be able to predict a jump in the first normal stress difference at the shear-band interface, and study whether this discontinuity will enhance the instability or not. In addition, to our knowledge, no previous theoretical work has studied the dependence of the second normal stress difference on these elastic instabilities present in channel flow, as the majority of the models are unable to predict a non-zero value of N_2. A model that can help us to achieve this is a recently published model [20] that couples the flow behaviour, structural parameters and diffusion of species, with full tensorial expressions derived from extended irreversible thermodynamics. Such a model (which is an even more general extension of the BMP model used in the present work) is also able to predict a non-zero second normal stress difference.

In order to prove the validity of our results, we would expect in a near future that experimental rheologists could be able to carry out experiments to study the stability of pressure-driven channel flow of thixotropic-viscoelasto-plastic fluids with and without shear-banding. Another challenging problem still pending is to address the true yield stress case for both zero and nonzero shear-banding cases. Finally, a fully comprehensive mechanism for the instabilities studied here is still elusive, though we have gained valuable insight through the current work.

Acknowledgements

This work was supported financially by the National Council of Science and Technology of Mexico (CONACyT Grant number: 299629 / 411301).

A Interfacial instabilities in channel flow of an Oldroyd-B fluid with concentration and Weissenberg number variable

We modify the governing equations used in [41] to adapt them to our problem. The set of equations is:

$$\underline{\nabla} \cdot \underline{u} = 0 \qquad \underline{\nabla} \cdot \underline{\underline{\sigma}} = 0 \tag{69}$$

$$\underline{\underline{\sigma}} = -p\underline{\underline{I}} + 2\underline{\underline{D}} + \frac{C}{W}\underline{\underline{A}} \qquad \overset{\nabla}{\underline{\underline{A}}} = -\frac{1}{W}(\underline{\underline{A}} - \underline{\underline{I}}) \tag{70}$$

$$\overset{\nabla}{\underline{\underline{A}}} = \frac{\partial \underline{\underline{A}}}{\partial t} + \underline{u} \cdot \underline{\nabla}\,\underline{\underline{A}} - \underline{\underline{A}} \cdot (\underline{\nabla}\,\underline{u}) - (\underline{\nabla}\,\underline{u})^{\top} \cdot \underline{\underline{A}}, \tag{71}$$

where $\underline{\underline{A}}$ and $\underline{\underline{I}}$ are the conformation and identity tensors, respectively. The other variables of the system are known and have been defined previously here. However, their definition slightly changes for this model; the concentration and the Weissenberg number are defined as:

$$W = \frac{\lambda_M U_0}{L} \qquad C = \frac{\lambda_M G_M U_0^2}{L^3 \mu}, \tag{72}$$

where λ_M and G_M are the relaxation time and elastic modulus, respectively, and μ is the solvent viscosity. These equations are used to study instabilities in pressure-driven channel flow, with the same geometry described in section 2.3.1, leading us to the following base-state equations:

$$C(y) = \begin{cases} C_1 & |y| > \kappa \\ C_2 & |y| < \kappa \end{cases} \qquad -\dot{\gamma}_0 = U' = Gy/[1 + C(y)] \tag{73}$$

$$G = -\mathcal{P} = \frac{-2(1 + C_1)(1 + C_2)}{(1 + C_1)\kappa^2 + (1 + C_2)(1 - \kappa^2)} \tag{74}$$

$$U(y) = \begin{cases} \dfrac{G(y^2 - 1)}{2(1 + C_1)}, & |y| > \kappa \\ \dfrac{G[(1 + C_1)(y^2 - \kappa^2) - (1 + C_2)(1 - \kappa^2)]}{2(1 + C_1)(1 + C_2)}, & |y| < \kappa \end{cases} \tag{75}$$

$$W(y) = \begin{cases} W_2 & |y| < \kappa \\ \left[\dfrac{(1 + C_1)}{(1 + C_2)}\right]^2 \left(\dfrac{C_2 W_2}{C_1}\right) & |y| > \kappa \end{cases} \tag{76}$$

$$\underline{\underline{\sigma}} = \begin{pmatrix} -Gx + 2\,C\,W(y)\,U'^{\,2} & Gy \\ Gy & -Gx \end{pmatrix} \qquad N_1 = 2\,C\,W(y)\,U'^{\,2} \tag{77}$$

Equation (73) shows the concentration profile $C(y)$, which is equivalent to our fluidity profile (30). Here, κ is the location of the interface where the two

fluids meet. Above this value of κ, the polymer will have a concentration of C_1, and below the interface it will have a value of C_2. In order to match these equations to our results, the viscosity (which is proportional to the polymer concentration) near the centreline C_2 has to be bigger than the one located near the wall, i.e. $C_2 \gg C_1$.

The shear rate $\dot{\gamma}_0$ can be calculated according to (73), and it is clearly seen that there will be a jump in $\dot{\gamma}_0$ at the interface κ, and this is due to the variation in the polymer concentration. The velocity profile obtained from the governing equations is shown in (75), and it also depends on the location of the interface. The coefficient G is the pressure gradient and is shown in (74). Unlike our velocity profiles reported in section 3.2, here G can be calculated analytically to satisfy $U(0) = 1$.

The most important difference between the equations used in this section and the ones used by Wilson & Rallison in [41] is that here we require continuity in the first normal stress difference N_1 to compare the results predicted by the Oldroyd-B model with the ones that were shown in section 4.1.1. In order to achieve that, we need a Weissenberg number that is different between the two fluids. Additionally, we have to find the values of W that satisfy the condition $[N_1] = 0$ at $y = \kappa$. The Weissenberg number profile $W(y)$ proposed is shown in equation (76), where W_2 stands for the Weissenberg number of the layer of fluid with concentration C_2, meanwhile the Weissenberg number for $y > \kappa$, W_1, depends on C_1, C_2, W_2 and the location of the interface. If the condition $C_2 > C_1$ is satisfied, W_2 will also be greater than W_1.

We show in figure 29 the velocity and first normal stress difference coefficient profiles along the channel calculated with equations (75) and (77). We choose parameter values that can provide us with a base state behaviour similar to the ones predicted by the generalised BMP model. For instance, the fluid viscosity near the centreline $(1 + C_2)$ is much higher than the viscosity near the channel wall $(1 + C_1)$. We also select a value of κ relatively near to the channel wall, and we fix $W_2 = 4$, giving us a value of $W_1 = 0.4744$ using equation (76).

We see that the velocity profile in figure 29a) resembles the one reported in figure 5a): we observe a plug-flow for values of channel coordinate $|y|$ below κ (dotted lines), and the velocity decreases rapidly as the coordinate approaches $|y| = 1$, which is where the polymer concentration C_1 is smaller. Furthermore, we can see that figure 29b) shows a smooth, parabolic and continuous first normal stress difference profile N_1 similar to the one predicted by the BMP model in figure 5c).

Now that we have demonstrated that these equations satisfy our conditions, we study the stability of layered Oldroyd-B fluids with differing concentration and Weissenberg number using a similar method described in sections 3.3 and 3.4.2: an infinitesimal perturbation ε is added to the base flow, and all the quantities from the governing equations (69)–(70) and the base state equations (73)–(77) are modified by a small change. The whole set of perturbed

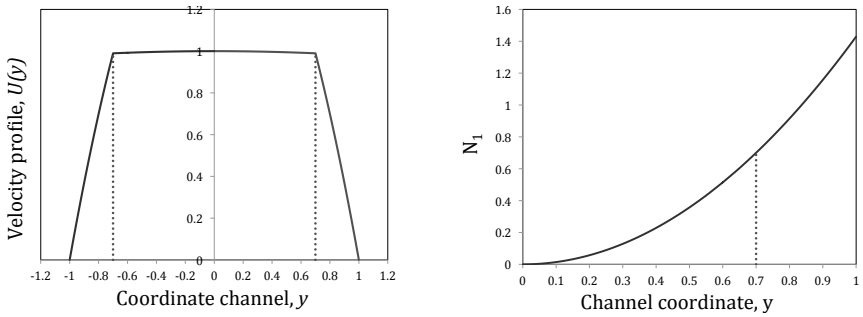

(a) Velocity profile

(b) Normal stress difference profile

Figure 29: Velocity (a) and first normal stress difference (b) profiles for an Oldroyd-B fluid with concentration and Weissenberg number variable. The parameters used are: $C_1 = 0.1$, $C_2 = 100$, $W_2 = 4$ and $\kappa = 0.7$ (vertical dotted lines).

governing equations can be found in [41]. We require non-slip boundary conditions at the channel-wall, boundary conditions for either sinuous or varicose modes (see section 3.4), and we must satisfy continuity of the velocity, shear rate and of the traction at the interface $y = \kappa + \zeta\varepsilon$. We show some results below.

We choose two values of interface location $\kappa = [0.7, 0.8]$, and using the same parameter values as the ones used in figure 29, we obtain the dispersion relation $\Im(\omega)$ vs k for those values of κ, which are depicted in figure 30a). Notice that the modes obtained are interfacial, as the growth rate becomes neutrally stable for long waves $k = 0$. As the wavenumber is increased, we see that the flow is stable and remains this way until we reach values of $k \approx 0.6$ for $\kappa = 0.7$ and $k \approx 0.81$ for $\kappa = 0.8$, where the flow becomes unstable. The growth rate reaches a maximum value and then will decrease until flow stability is seen again.

Furthermore, the elasticity of the fluid seems to play a key role in the interfacial instability. If we keep the same parameter values $C_1 = 0.1$, $C_2 = 100$ and $\kappa = [0.7, 0.8]$ fixed, and now we decrease the Weissenberg number to $W_2 = 1$, we obtain figure 30b), and the modes are completely stable for the same range of values of k where an instability is observed in 30a).

The main conclusion here is that an interfacial instability exists indeed and is predicted by the BMP model and the Oldroyd-B model, given the proper flow conditions, i.e. a jump in the fluid viscosity at the interface, along with continuity in the first normal stress difference. However, there are still some remarkable differences between the interfacial modes shown in section 4.1.2 and the ones from figure 30. For instance, for the modes predicted by the generalised BMP model (see figure 10), we always observe that the growth rate remains positive, and reaches an asymptotic value for large values of wavenumber, in

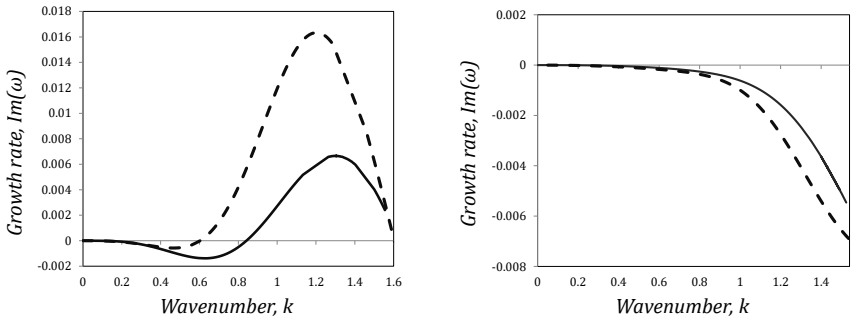

(a) Unstable flows (b) Stable flows

Figure 30: Dispersion relation $\Im(\omega)$ vs k for sinuous modes of an Oldroyd-B fluid with polymer concentration and Weissenberg number variable. The parameter values used are: $C_1 = 0.1$ and $C_2 = 100$. For both plots, dashed lines indicate an interface location at $\kappa = 0.7$. Solid lines: $\kappa = 0.8$. Figure (a): $W_2 = 4$, $W_1 = 0.4745$ unstable modes. Figure (b): $W_2 = 1$, $W_1 = 0.1186$ stable modes.

contrast to the modes shown in 30. These dissimilarities might be due to model characteristics; for instance, the effect of solvent viscosity in the Oldroyd-B model in equation (70), which is something that we are ignoring for the BMP model. Perhaps more important is that in the BMP model there is shear-thinning within each phase, whereas the Oldroyd-B model has constant shear viscosity.

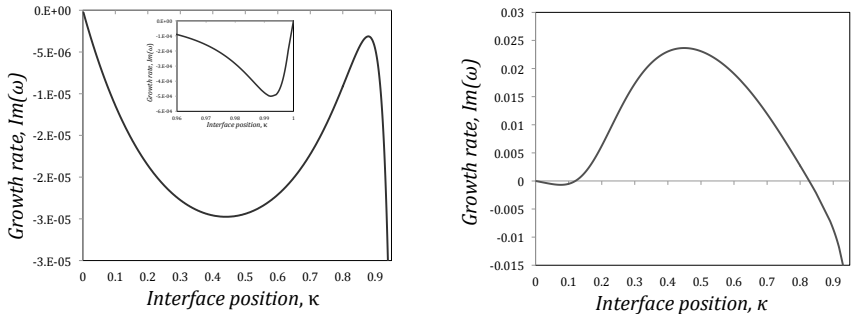

(a) $k = 0.1$ (b) $k = 1$

Figure 31: Growth rate $\Im(\omega)$ against interface location κ for sinuous modes, with $C_1 = 0.1$, $C_2 = 100$, and $W_2 = 4$ fixed. Figure (a): longwaves $k = 0.1$. The small plot shows the behaviour near the wall. Figure (b): $k = 1$.

In figure 31 we show two cases of growth rate against interface position for the Oldroyd-B model. The parameter values used are the same as those from figure 30, but here we fix the wavenumber. For long waves (figure 31a) we can

see that the flow is always stable, independently of the value of κ, and the mode is neutrally stable if there is no fluid interface within the channel ($\kappa = 0$ or $\kappa = 1$). Something similar is observed for the case $k = 1$ in figure 31b), but the main difference with respect to the long wave case is that an instability is observed for an interval of $0.12 < \kappa < 0.81$. In section 3.1, we saw that this is another difference between the modes predicted by the Oldroyd-B and the BMP model, which is that for the latter it is not possible for us to specify κ, and the interfacial modes will only exist for appropriate parameter values that lead to the formation of bands.

References

[1] D. Acierno, F. P. La Mantia, G. Marrucci and G. Titomanlio. A non-linear viscoelastic model with structure-dependent relaxation times: I. Basic formulation. *Journal of Non-Newtonian Fluid Mechanics*, 1(2):125–146, 1976.

[2] F. Bautista, J. M. De Santos, J. E. Puig and O. Manero. Understanding thixotropic and antithixotropic behavior of viscoelastic micellar solutions and liquid crystalline dispersions. I. The model. *Journal of Non-Newtonian Fluid Mechanics*, 80(2-3):93–113, 1999.

[3] F. Bautista, J. F. A. Soltero, J. H. Pérez-López, J. E. Puig and O. Manero. On the shear banding flow of elongated micellar solutions. *Journal of Non-Newtonian Fluid Mechanics*, 94(1):57–66, 2000.

[4] J.-F. Berret, D. C. Roux, G. Porte and P. Lindner. Shear-induced isotropic-to-nematic phase transition in equilibrium polymers. *EPL (Europhysics Letters)*, 25(7):521, 1994.

[5] P. T. Callaghan, M. E. Cates, C. J. Rofe and J. B. A. F. Smeulders. A study of the "Spurt Effect" in wormlike micelles using Nuclear Magnetic Resonance Microscopy. *Journal de Physique II*, 6(3):375–393, 1996.

[6] L. Casanellas, C. J Dimitriou, T. J. Ober and G. H. McKinley. Spatiotemporal dynamics of multiple shear-banding events for viscoelastic micellar fluids in cone-plate shearing flows. *Journal of Non-Newtonian Fluid Mechanics*, 222:234–247, 2015.

[7] H. A. Castillo, J. C. Tejas, J. P. García-Sandoval, O. Matus, F. Bautista, J. E. Puig and O. Manero. Derivation of the mechanical and thermodynamic potentials from the generalized BMP model under shear-banding flow. *Journal of Non-Equilibrium Thermodynamics*, 39(4):231–248, 2014.

[8] H. A Castillo and H. J. Wilson. Towards a mechanism for instability in channel flow of highly shear-thinning viscoelastic fluids. *Journal of Non-Newtonian Fluid Mechanics*, 247:15–21, 2017.

[9] H. A. Castillo and H. J. Wilson. Elastic instabilities in pressure-driven channel flow of thixotropic-viscoelasto-plastic fluids. *Journal of Non-Newtonian Fluid Mechanics*, 261:10–24, 2018.

[10] K. Chen. Elastic instability of the interface in Couette flow of viscoelastic liquids. *Journal of Non-Newtonian Fluid Mechanics*, 40(2):261–267, 1991.

[11] M. Cromer, L. P. Cook and G. H. McKinley. Interfacial instability of pressure-driven channel flow for a two-species model of entangled wormlike micellar solutions. *Journal of Non-Newtonian Fluid Mechanics*, 166(11):566–577, 2011.

[12] J. P. Decruppe, R. Cressely, R. Makhloufi and E. Cappelaere. Flow birefringence experiments showing a shear-banding structure in a CTAB solution. *Colloid and Polymer Science*, 273(4):346–351, 1995.

[13] J. I. Escalante, E. R. Macias, F. Bautista, J. H. Pérez-López, J. F. A. Soltero, J. E. Puig and O. Manero. Shear-banded flow and transient rheology of cationic wormlike micellar solutions. *Langmuir*, 19(17):6620–6626, 2003.

[14] R. H. Ewoldt and G. H. McKinley. Mapping Thixo-Visco-Elasto-Plastic behavior. *Rheological Acta*, 256:195–210, 2017.

[15] M.-A. Fardin, L. Casanellas, B. Saint-Michel, S. Manneville and S. Lerouge. Shear-banding in wormlike micelles: Beware of elastic instabilities. *Journal of Rheology*, 60(5):917–926, 2016.

[16] S. M. Fielding. Linear instability of planar shear banded flow. *Physical Review Letters*, 95(13):134501, 2005.

[17] S. M. Fielding. Viscoelastic Taylor-Couette instability of shear banded flow. *Physical Review Letters*, 104(19):198303, 2010.

[18] S. M. Fielding and H. J. Wilson. Shear banding and interfacial instability in planar Poiseuille flow. *Journal of Non-Newtonian Fluid Mechanics*, 165(5-6):196–202, 2010.

[19] A. G. Fredrickson. A model for the thixotropy of suspensions. *AIChe journal*, 16(3):436–441, 1970.

[20] J. P. García-Sandoval, F. Bautista, J. E. Puig and O. Manero. Inhomogeneous flow of wormlike micelles: predictions of the generalized BMP model with normal stresses. *Fluids*, 4(1):45, 2019.

[21] S. J. Haward, F. J. Galindo-Rosales, P. Ballesta and M. A. Alves. Spatiotemporal flow instabilities of wormlike micellar solutions in rectangular microchannels. *Applied Physics Letters*, 104(12):124101, 2014.

[22] E. J. Hinch, O. J. Harris and J. M. Rallison. The instability mechanism for two elastic liquids being co-extruded. *Journal of Non-Newtonian Fluid Mechanics*, 43(2-3):311–324, 1992.

[23] T. C. Ho and M. M. Denn. Stability of plane Poiseuille flow of a highly elastic liquid. *Journal of Non-Newtonian Fluid Mechanics*, 3(2):179–195, 1977.

[24] W. M. Holmes, M. R. Lopez-Gonzalez and P. T. Callaghan. Fluctuations in shear-banded flow seen by NMR velocimetry. *Europhysics Letters*, 64(2):274, 2003.

[25] Y. Kim, A. Adams, W. H. Hartt, R. G. Larson and M. J. Solomon. Transient, near-wall shear-band dynamics in channel flow of wormlike micelle solutions. *Journal of Non-Newtonian Fluid Mechanics*, 232:77–87, 2016.

[26] R. G. Larson. A constitutive equation for polymer melts based on partially extending strand convection. *Journal of Rheology*, 28(5):545–571, 1984.

[27] S. Lerouge, M. Argentina and J.-P. Decruppe. Interface instability in shear-banding flow. *Physical Review Letters*, 96(8):088301, 2006.

[28] M. P. Lettinga and S. Manneville. Competition between shear banding and wall slip in wormlike micelles. *Physical Review Letters*, 103(24):248302, 2009.

[29] M. R. López-González, W. M. Holmes and P. T. Callaghan. Rheo-NMR phenomena of wormlike micelles. *Soft Matter*, 2(10):855–869, 2006.

[30] M. R. López-González, W. M. Holmes, P. T. Callaghan and P. J. Photinos. Shear banding fluctuations and nematic order in wormlike micelles. *Physical Review Letters*, 93(26):268302, 2004.

[31] R. W. Mair and P. T. Callaghan. Observation of shear banding in worm-like micelles by NMR velocity imaging. *EPL (Europhysics Letters)*, 36(9):719, 1996.

[32] O. Manero, J. H. Pérez-López, J. I. Escalante, J. E. Puig and F. Bautista. A thermodynamic approach to rheology of complex fluids: The generalized bmp model. *Journal of Non-Newtonian Fluid Mechanics*, 146(1-3):22–29, 2007.

[33] S. Manneville, L. Bécu and A. Colin. High-frequency ultrasonic speckle velocimetry in sheared complex fluids. *The European Physical Journal-Applied Physics*, 28(3):361–373, 2004.

[34] H. Mohammadigoushki and S. J. Muller. A flow visualization and superposition rheology study of shear-banding wormlike micelle solutions. *Soft Matter*, 12(4):1051–1061, 2016.

[35] P. Nghe, S. M. Fielding, P. Tabeling and A. Ajdari. Interfacially driven instability in the microchannel flow of a shear-banding fluid. *Physical Review Letters*, 104(24):248303, 2010.

[36] A. Nicolas and A. Morozov. Nonaxisymmetric instability of shear-banded Taylor-Couette flow. *Physical Review Letters*, 108(8):088302, 2012.

[37] M. Renardy. The mathematics of myth: Yield stress behavior as a limit of non-monotone constitutive theories. *Journal of Non-Newtonian Fluid Mechanics*, 165(9-10):519–526, 2010.

[38] Y. Renardy and M. Renardy. Stability of shear banded flow for a viscoelastic constitutive model with thixotropic yield stress behavior. *Journal of Non-Newtonian Fluid Mechanics*, 244:57–74, 2017.

[39] H. J. Wilson and S. M. Fielding. Linear instability of planar shear banded flow of both diffusive and non-diffusive Johnson–Segalman fluids. *Journal of Non-Newtonian Fluid Mechanics*, 138(2-3):181–196, 2006.

[40] H. J. Wilson and V. Loridan. Linear instability of a highly shear-thinning fluid in channel flow. *Journal of Non-Newtonian Fluid Mechanics*, 223:200–208, 2015.

[41] H. J. Wilson and J. M. Rallison. Instability of channel flows of elastic liquids having continuously stratified properties. *Journal of Non-Newtonian Fluid Mechanics*, 85(2-3):273–298, 1999.

[42] T. Yamamoto, T. Hashimoto and A. Yamashita. Flow analysis for wormlike micellar solutions in an axisymmetric capillary channel. *Rheologica Acta*, 47(9):963–974, 2008.